

AD-A118 883

OHIO STATE UNIV COLUMBUS ELECTROSCIENCE LAB

F/G 9/5

THE HIGH-FREQUENCY RADIATION PATTERNS OF A SPHEROID-MOUNTED ANT--ETC(U)

MAR 80 C C HUANG, N WANG, W D BURNSIDE

N00019-80-C-0050

UNCLASSIFIED

ESL-712527-1

NL

10-1  
4-2  
10-1

END  
DATE  
FILMED  
10-82  
DTIC

AD A118883

UNCLASSIFIED

SECURITY CLASSIFICATION OF THIS PAGE (When Data Entered)

REPORT DOCUMENTATION PAGE		READ INSTRUCTIONS BEFORE COMPLETING FORM
1. REPORT NUMBER	2. GOVT ACCESSION NO.	3. RECIPIENT'S CATALOG NUMBER
	AD A118883	
4. TITLE (and Subtitle)		5. TYPE OF REPORT & PERIOD COVERED
THE HIGH-FREQUENCY RADIATION PATTERNS OF A SPHEROID-MOUNTED ANTENNA		Quarterly Report 11/29/79 - 2/29/80
7. AUTHOR(s)		6. PERFORMING ORG. REPORT NUMBER
C. C. Huang N. Wang W. D. Burnside		ESL 712527-1
9. PERFORMING ORGANIZATION NAME AND ADDRESS		8. CONTRACT OR GRANT NUMBER(s)
The Ohio State University ElectroScience Laboratory, Department of Electrical Engineering, Columbus, Ohio 43212		Contract N00019-80-C-0050
11. CONTROLLING OFFICE NAME AND ADDRESS		10. PROGRAM ELEMENT, PROJECT, TASK AREA & WORK UNIT NUMBERS
Department of the Navy Naval Air Systems Command Washington, D. C. 20361		
14. MONITORING AGENCY NAME & ADDRESS (if different from Controlling Office)		12. REPORT DATE
		March 1980
		13. NUMBER OF PAGES
		79
		15. SECURITY CLASS. (of this report)
		Unclassified
		16a. DECLASSIFICATION/DOWNGRADING SCHEDULE
16. DISTRIBUTION STATEMENT (of this Report)		
APPROVED FOR PUBLIC RELEASE DISTRIBUTION UNLIMITED		
17. DISTRIBUTION STATEMENT (of the abstract entered in Block 20, if different from Report)		
18. SUPPLEMENTARY NOTES		
The material contained in this report is also used as a thesis submitted to the Department of Electrical Engineering, The Ohio State University as partial fulfillment for the degree Master of Science.		
19. KEY WORDS (Continue on reverse side if necessary and identify by block number)		
Electromagnetic radiation                      Prolate spheroid mounted antenna High frequency solutions                      Comparisons with measurements Geometrical Theory of Diffraction Perturbation methods		
20. ABSTRACT (Continue on reverse side if necessary and identify by block number)		
<p>→ An efficient numerical solution for the high frequency radiation patterns of a spheroid-mounted antenna is investigated. The Geometrical Theory of Diffraction is the basic approach applied here. The ray analysis in the lit region is straightforward; whereas, the geodesic paths on the surface dictate whether the shadow region solution is practical to obtain or not. Previous attempts employing calculus of variations or tensor analysis were too complicated to use. Cylinder</p>		

DD FORM 1 JAN 73 1473

EDITION OF 1 NOV 65 IS OBSOLETE

UNCLASSIFIED

SECURITY CLASSIFICATION OF THIS PAGE (When Data Entered)

UNCLASSIFIED

SECURITY CLASSIFICATION OF THIS PAGE(When Data Entered)

20.

and cone perturbation methods are presented to simulate the geodesic paths on a spheroid, which in turn can be used to model an aircraft or missile fuselage. The geodesic paths are then efficiently solved via a numerical approach, in that a cylinder and cone are developed surfaces.

Good agreement between the measurement and calculation results has been obtained except when caustic effects come into play. This type of caustic effect is still an unsolved problem and is beyond the scope of the present study. This study has presented a very useful solution in approximating the geodesic paths on a spheroid, and predicting the high frequency radiation patterns for spheroid-mounted antennas. Using this perturbation approach one can extend this technique to solve for the geodesic paths on more complex convex surfaces.

Accession For	
NTIS GRA&I	<input checked="checked" type="checkbox"/>
DTIC TAB	<input type="checkbox"/>
Unannounced	<input type="checkbox"/>
Justification	
By	
Distribution/	
Availability Codes	
Dist	Avail and/or Special
A	

COPY

REMOVED

UNCLASSIFIED

SECURITY CLASSIFICATION OF THIS PAGE(When Data Entered)

## ACKNOWLEDGEMENT

The author would like to express his special thanks to his graduate adviser, Professor W. D. Burnside, for the considerable assistance he has provided. Dr. N. Wang and Dr. P. H. Pathak also deserve gratitude for their discussions. Professor L. Peters, Jr. has been helpful in reviewing the author's manuscript. His valuable criticism is appreciated. The work reported in this thesis was supported by Naval Air Systems Command under Contract N00019-80-C-0050.

## TABLE OF CONTENTS

	Page
ACKNOWLEDGEMENTS.....	11
Chapter	
I    INTRODUCTION.....	1
II   THEORETICAL BACKGROUND.....	6
Introduction	
Shadow Region	
Lit Region	
Pattern Factors	
Spheroid Surface Parameters	
III  NUMERICAL TECHNIQUE AND PERTURBATION METHOD.....	23
Introduction	
Surface Geodesics	
Cylinder Perturbation	
Cone Perturbation	
IV   RESULTS.....	45
V    SUMMARY AND CONCLUSIONS.....	78
REFERENCES.....	79

## CHAPTER 1

### INTRODUCTION

The object of this study is to develop an efficient numerical solution for the high-frequency radiation patterns of a spheroid-mounted antenna. The Geometrical Theory of Diffraction (GTD) is employed for the pattern calculation of which the creeping wave [1] solution in the shadow region is of particular interest here. According to the generalized Fermat's principle, a ray emanating from a source, which is located on the surface, follows a geodesic path on the surface and continually sheds energy into the shadow region. Such a creeping wave mechanism is illustrated in Figure 1(a), from which it can be seen that a ray traverses from the source point  $Q'$  to the diffraction point  $Q$ , and then propagates along the geodesic tangent at  $Q$  toward the observation point  $P_s$ . Since most parameters involved in the pattern calculation are related to the ray path, the geodesic solution on the surface constitutes a major portion of this study.

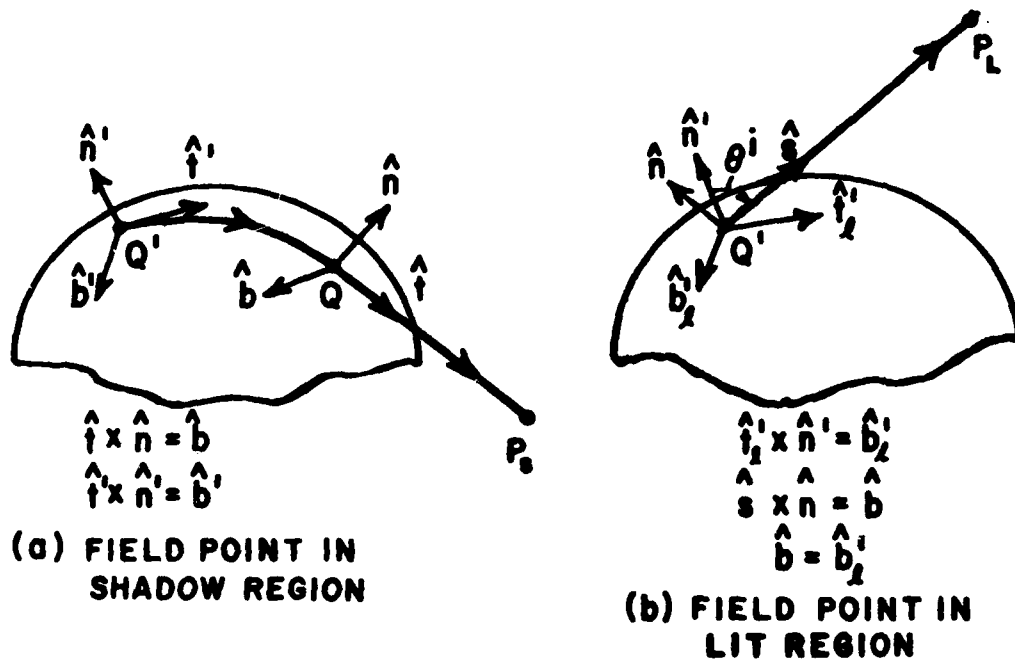


Figure 1. Ray paths in the shadow and lit regions.

The spheroid is studied because of its three dimensional nature in that it can be used to simulate an aircraft or missile fuselage. For a flush-mounted airborne antenna, the fuselage has a dominant effect on the resulting radiation pattern. Previously [2] the fuselage was simulated by an elliptic cylinder; however, the cylinder model could not predict the pattern close to the nose or tail sectors, where the deviation from the physical situation becomes very prominent. Previous attempts [2], using the spheroid model, employed calculus of variations or tensor analysis to calculate the geodesic paths. The resulting algorithms were very time-consuming and virtually impractical to use. Therefore, a perturbation method is presented here in an attempt to combine the simplicity of the cylinder or cone solution with the generality of the prolate spheroid.

Before examining our perturbation approach, it is appropriate to study the basic radiation mechanisms in some detail in that they suggest the present solution. The ray analysis in the lit region can be rather straightforwardly analyzed for any convex surface; however, the geodesics which are necessary to treat the shadow region dictate what surfaces can be efficiently analyzed. In the shadow region, the energy propagates outward from the source along the geodesic paths. As the energy flows around the surface, it is continuously diffracted along the geodesic tangent toward the field point such that the significant effect of the surface is associated with a region around the source. In fact, for a prolate spheroid, the significant portion of the surface, which is associated with the dominant energy, may look as shown in Figure 2. Note that this region can be specified by following the various geodesic paths until the radiation level along a given path becomes insignificant, i.e., more than 40 db below the pattern maximum. With this in mind, it is clear that one could represent the prolate spheroid by a structure which simulates the circular cross-section completely; however, the profile (i.e., the elliptic curve) could be approximated by a simpler shape in that the significant energy region does not cover a large portion of the profile shape. Consequently, a right circular cone perturbation is chosen here to simulate the spheroid which in turn can be used to model a fuselage. This perturbation model is illustrated in Figure 3 for a source located near one end of the spheroid. Note that if the antenna is placed at the center of the spheroid, the cone actually becomes a right circular cylinder.

In that the cone is a developed surface, one can unfold the cone such that a planar structure results. The geodesics associated with the cone are, then, straight lines on this planar structure. In order to allow for a geodesic solution between the simplicity of the cone and the rigor of the spheroid, one can perturb the cone by bending it along its generator as illustrated in Figure 3(b). In that a perturbation technique is employed, the geodesic paths for the cone are simply modified such that the solution for the spheroid is basically straightforward and is the basis for this thesis. It is obvious that one cannot use this perturbation if significant energy propagates great



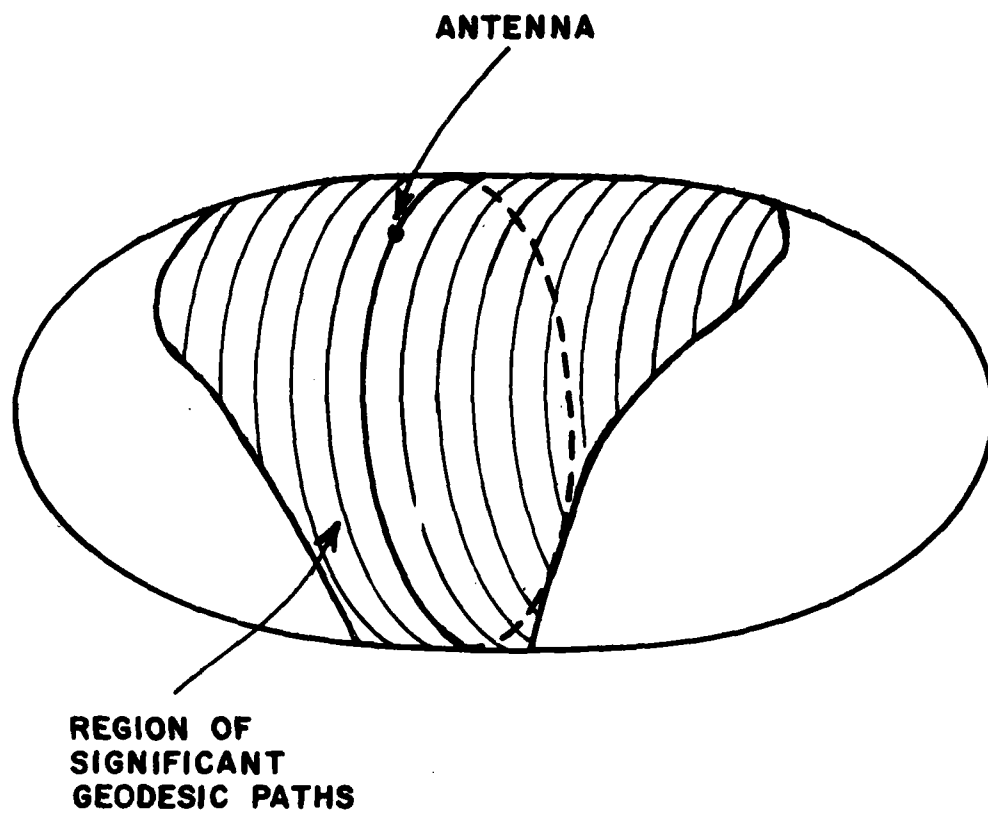


Figure 2. The region of significant energy flow from an antenna mounted on a prolate spheroid.

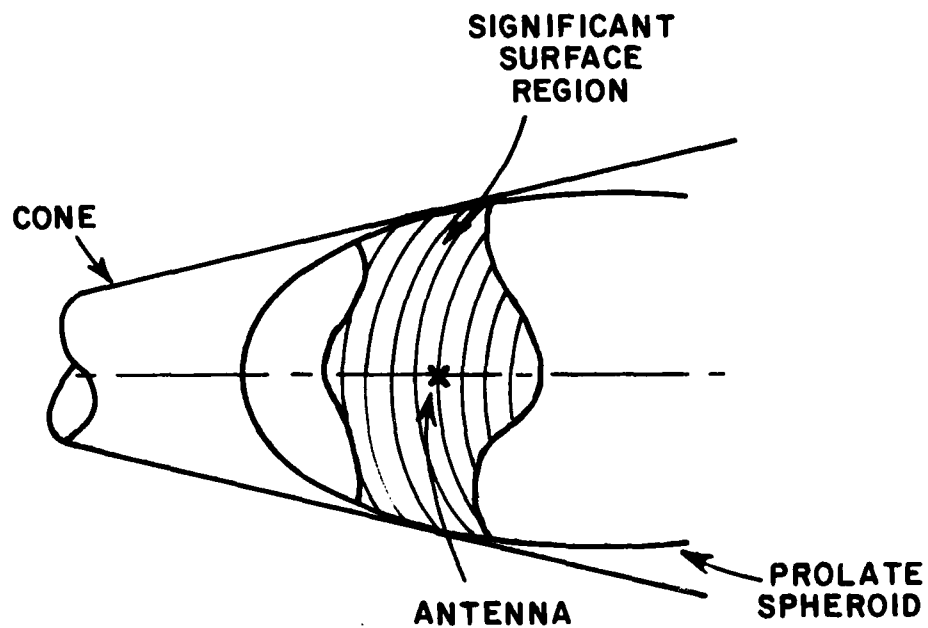


Figure 3(a). Cone simulation.

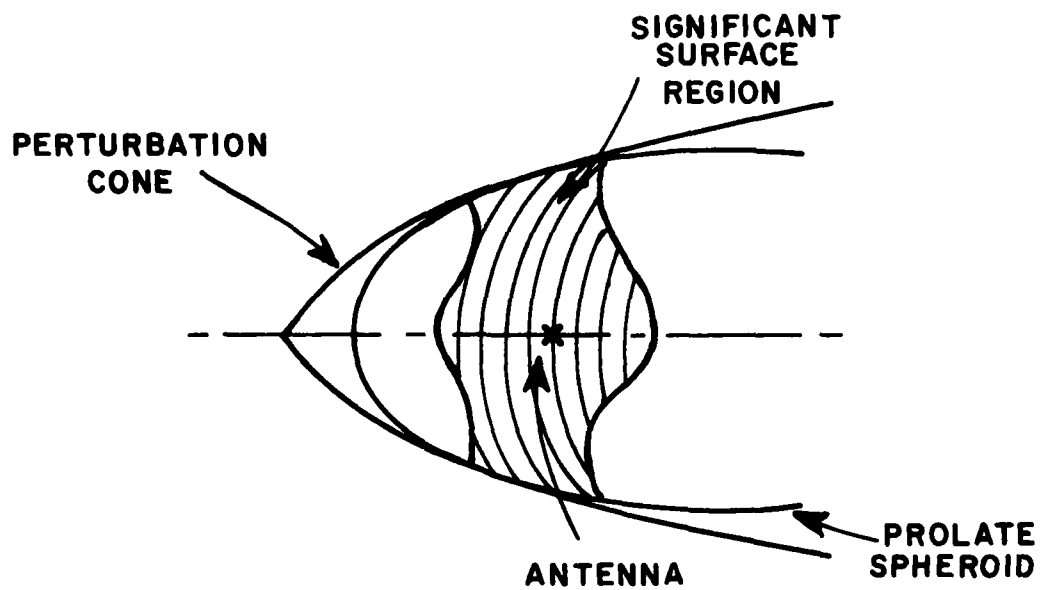


Figure 3(b). Cone perturbation model.

distances along the surface. However, as discussed above, the energy which propagates great distances along the spheroid generator becomes insignificant in magnitude such that one need not solve for the true geodesic paths outside the region shown in Figure 3. The simplicity of these perturbed geodesic paths allows one to very efficiently determine the significant ray paths on the prolate spheroid.

It is noted that, since GTD is a high-frequency method, the lower frequency limit of this solution is dictated by the electrical dimensions of the spheroid, i.e., the semi-minor axis of the spheroid is required to be at least a wavelength.

The curved surface diffraction solutions employed here are briefly discussed in Chapter II. The parameters needed for this GTD solution are described in Chapter III in terms of the cylinder and cone perturbations used to simulate the geodesic paths on the spheroid. Analytic results are compared with various measurements in Chapter IV. Finally, a summary of this study is made in Chapter V.

## CHAPTER II

### THEORETICAL BACKGROUND

#### A. INTRODUCTION

The radiated field of a spheroid-mounted antenna is analyzed using the Geometrical Theory of Diffraction (GTD). The surface is assumed to be perfectly conducting, and the surrounding medium is free space. An  $\exp(j\omega t)$  time dependence is understood and suppressed in the following formulations.

Consider an infinitesimal, magnetic current moment  $d\vec{P}_m(Q')$  or an electric current moment  $d\vec{P}_e(Q')$  located on a perfectly conducting convex surface as shown in Figure 1; the sources

$$d\vec{P}_m(Q') = \vec{E}(Q') \times \hat{n}' da'$$

$$\text{and } d\vec{P}_e(Q') = I(\ell') d\ell' \hat{n}'$$

pertain to the aperture and monopole type excitations with

$\vec{E}(Q')$  = electric field at  $Q'$ ,

$\hat{n}'$  = outward unit surface normal at  $Q'$ ,

$da'$  = area element at  $Q'$ ,

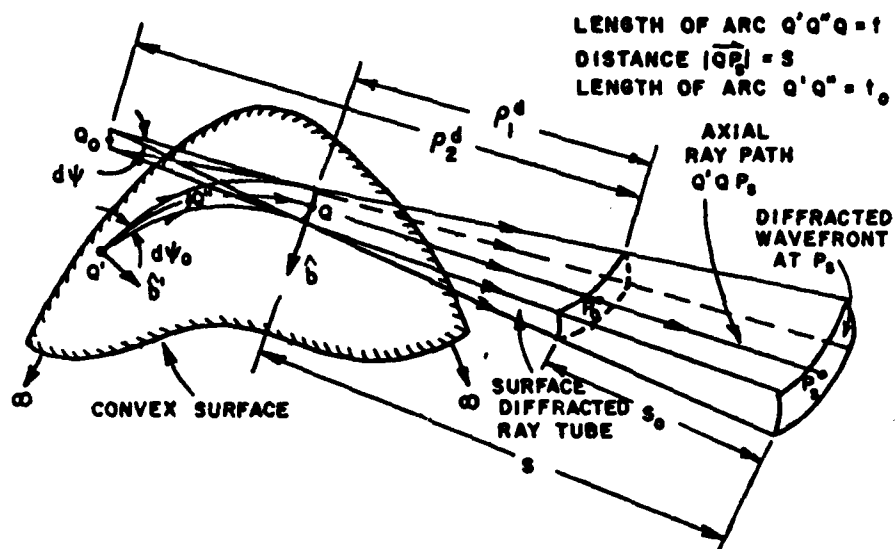
$I(\ell')$  = electric current distribution on the monopole, and

$\ell'$  = distance parameter along the monopole.

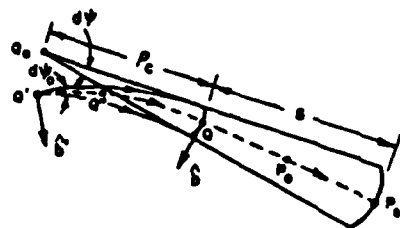
According to geometrical optics, the space surrounding the source is divided into an illuminated and shadow region by a plane tangent to the surface at  $Q'$ . This plane is referred to as a shadow boundary. Since the field in the deep lit region is essentially that obtained from geometrical optics, and the field in the deep shadow region is relatively weak, the solution for the transition region adjacent to the shadow boundary is of more interest and discussed below.

#### B. SHADOW REGION

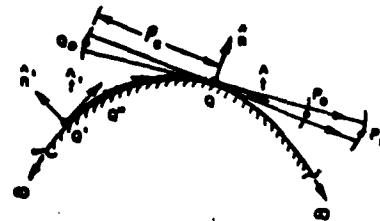
The creeping wave mechanism in the shadow region is illustrated in Figure 4. From the generalized Fermat's principle, a ray emanating



(a) Perspective view of a surface diffracted ray tube (enlarged view).



(b) Top view of diffracted ray tube indicating the divergence of the rays and the unit binormal vectors at  $Q'$  and  $Q$ .



(c) Side view of surface diffracted ray tube and the unit normal and tangent vectors at  $Q'$  and  $Q$ .

Figure 4. Surface diffracted ray tube and ray coordinates for the shadow region.

from the source  $d\bar{P}_m(Q')$  at  $Q'$  traverses a geodesic path  $Q'O$  on the surface, and propagates along the geodesic tangent at  $Q$  toward the field point  $P_s$ . The field  $d\bar{E}_m$  at  $P_s$  can be expressed in terms of the field at a reference point  $P_0$  by [3]

$$d\bar{E}_m(P_s) \sim d\bar{E}_m(P_0) \sqrt{\frac{\rho_1^d \rho_2^d}{(\rho_1^d + s_0)(\rho_2^d + s_0)}} e^{-jks_0 + O[m^{-2}, m^{-3}]} \quad (1)$$

where

$\rho_1^d$  and  $\rho_2^d$  are the principal radii of curvatures of the wavefront at  $P_0$ ;

and  $O[m^{-2}, m^{-3}, \dots]$  are the higher order terms.

From Figure 4, it is seen that if the reference point  $P_0$  is moved to the curved surface diffraction point  $Q$ , then  $\rho_1^d \rightarrow 0$ ,  $\rho_2^d \rightarrow \rho_c$ , and  $s_0 \rightarrow s$ . Since  $d\bar{E}_m(P_s)$  is independent of the reference point  $P_0$ , it follows that

$$\lim_{\substack{P_0 \rightarrow Q \\ \rho_1^d \rightarrow 0}} \sqrt{\rho_1^d} d\bar{E}_m(P_0) = \bar{L}_m(Q', Q) \quad ; \quad (2)$$

then,

$$d\bar{E}_m(P_s) \sim \bar{L}_m(Q', Q) \sqrt{\frac{\rho_c}{s(\rho_c + s)}} e^{-jks} \quad (3)$$

Furthermore,  $\bar{L}_m(Q', Q)$  can be related to the source strength  $d\bar{P}_m$  at  $Q'$  by

$$\bar{L}_m(Q', Q) = d\bar{P}_m(Q') \cdot \bar{T}_m(Q', Q) \quad (4)$$

where  $\bar{T}_m(Q', Q)$  is given by [3]

$$\bar{T}_m(Q', Q) = \frac{-jk}{4\pi} [\hat{b}' \hat{n} T_1(Q') H + \hat{t}' \hat{b} T_2(Q') S + \hat{b}' \hat{b} T_3(Q') S + \hat{t}' \hat{n} T_4(Q') H]$$

$$e^{-jkt} \sqrt{\frac{d\psi_0}{d\eta(Q)}} \left[ \frac{\rho_g(Q)}{\rho_g(Q')} \right]^{1/6} \quad (5)$$

$$\bar{T}_e(Q', Q) = \frac{-jkZ_0}{4\pi} [\hat{n}' \hat{n} T_5(Q') H + \hat{n}' \hat{b} T_6(Q') S] e^{-jkt}$$

$$\sqrt{\frac{d\psi_0}{d\eta(Q)}} \left[ \frac{\rho_g(Q)}{\rho_g(Q')} \right]^{1/6} \quad (6)$$

Here  $(\hat{t}', \hat{n}', \hat{b}')$  and  $(\hat{t}, \hat{n}, \hat{b})$  are the tangent, normal and binormal unit vectors to the surface at the source point  $(Q')$  and diffraction point  $(Q)$ , respectively. As seen from Figure 4,  $\hat{t} \times \hat{n} = \hat{b}$  and  $\hat{t}' \times \hat{n}' = \hat{b}'$ . The quantities  $T_1(Q'), \dots, T_6(Q')$  are the torsion factors at  $Q'$  and are given in Table 1. Also,

$$H = g(\xi) \quad (7)$$

$$S = \frac{-j}{m(Q')} \tilde{g}(\xi) \quad (8)$$

with

$$g(\xi) = \frac{1}{\sqrt{\pi}} \int_{-\infty \exp(-j2\pi/3)}^{\infty} d\tau \frac{\exp(-j\tau\xi)}{w_2'(\tau)} \quad \text{and} \quad (9)$$

$$\tilde{g}(\xi) = \frac{1}{\sqrt{\pi}} \int_{-\infty \exp(-j2\pi/3)}^{\infty} d\tau \frac{\exp(-j\tau\xi)}{w_2(\tau)} \quad (10)$$

which are known as the acoustic hard and soft Fock functions. The Fock type Airy function is given by

$$w_2(\tau) = \frac{1}{\sqrt{\pi}} \int_{-\infty \exp(j2\pi/3)}^{\infty} dt \cdot \exp(\tau t - t^3/3) \quad (11)$$

TABLE I (FOR SHADOW REGION)

TYPE OF CONVEX SURFACE	SLOT OR $\delta \bar{\rho}_0$ CASE			MONOPOLE OR $\delta \bar{\rho}_0$ CASE		SURFACE RAY TORSION $\tau_{10}'$	SURFACE RADIUS OF CURVATURE IN $\hat{\tau}_1$ DIRECTION $\rho_p(q')$	SURFACE DIFFRACTED RAY CAUSTIC DISTANCE $\rho_c$
	$\tau_{10}'$	$\tau_2(0')$	$\tau_3(0')$	$\tau_4(0')$	$\tau_6(0')$			
SPHERE	1	1	0	0	1	0	0	$\sin(\frac{1}{2})$
CIRCULAR CYLINDER	1	1	$\frac{\sin 2\alpha'}{2\alpha'} \cdot \frac{a}{\sin^2 \alpha'}$	0	1	$\frac{\sin 2\alpha'}{2\alpha'} \cdot \frac{a}{\sin^2 \alpha'}$	$\frac{a}{\sin^2 \alpha'}$	1
ARBITRARY CONVEX SURFACE	1	1	$\tau_{10}' \rho_p(0')$	0	1	$\tau_{10}' \rho_p(0')$	$\frac{\sin 2\alpha'}{2} \left( \frac{1}{\rho_p(0')} - \frac{1}{\rho_c(0')} \right) \left( \frac{\cos^2 \alpha'}{n_1(0')} \cdot \frac{\sin^2 \alpha'}{n_2(0')} \right)^{-1}$ WITH $n_1(0') \neq n_2(0')$	$\frac{2\sqrt{E}}{2\alpha'/\alpha'}$

Note: (1)  $\alpha'$  is defined by  $\hat{\tau}_1 \cdot \hat{\tau}' = \cos \alpha'$  where  $\hat{\tau}_1$  is the principal direction unit vector associated with  $R_1(q')$ .

(2) The quantities E and G denote two of the three coefficients E, F, G that appear in the "first fundamental form" of Differential Geometry [4].



and  $w_2'(\tau)$  is the derivative of  $w_2(\tau)$  with respect to  $\tau$ . The Fock parameter  $\xi$  for the shadow region is given by [3]

$$\xi = \int_{Q'}^Q dt' \frac{m(t')}{\rho_g(t')} \quad (12)$$

with

$$m(t') = \left[ \frac{k \rho_g(t')}{2} \right]^{1/3} \quad (13)$$

Here  $\rho_g(t')$  is the surface radius of curvature along the ray path at  $t'$ . The width of the surface ray tube at  $Q$ ,  $d\eta(Q)$ , is given by

$$d\eta(Q) = \rho_c d\psi \quad (14)$$

The parameters  $Z_0$  and  $t$  are defined as the free space wave impedance and geodesic arc length from  $Q'$  to  $Q$ , respectively.

Combining Equations (3)-(14), the  $\hat{n}$  and  $\hat{b}$  directed components of  $dE_m(P_s)$  are given by [3]

(a)  $d\vec{P}m(Q')$  case:

$$dE_m^n(P_s) = \frac{-jk}{4\pi} (d\vec{P}m \cdot \hat{b}') H_e^{-jkt} \left[ \frac{\rho_g(Q')}{\rho_g(Q)} \right]^{-1/6} \sqrt{\frac{d\psi_0}{d\psi}} \sqrt{\frac{1}{s(\rho_c + s)}} e^{-jks + O[m^{-2}]} \quad (15)$$

$$dE_m^b(P_s) = \frac{-jk}{4\pi} [(d\vec{P}m \cdot \hat{b}) T_0 S + (d\vec{P}m \cdot \hat{t}') S] e^{-jkt} \left[ \frac{\rho_g(Q')}{\rho_g(Q)} \right]^{-1/6} \sqrt{\frac{d\psi_0}{d\psi}} \sqrt{\frac{1}{s(\rho_c + s)}} e^{-jks + O[m^{-2}, m^{-3}]} \quad (16)$$

(b)  $d\bar{P}_e(Q')$  case:

$$dE_e^n(P_s) = \frac{-jkZ_0}{4\pi} dP_e(Q') He^{-jkt} \left[ \frac{\rho_g(Q')}{\rho_g(Q)} \right]^{-1/6} \sqrt{\frac{d\psi_0}{d\psi}} \sqrt{\frac{1}{s(\rho_c+s)}} e^{-jks+0[m^{-2}]} \quad (17)$$

$$dE_e^b(P_s) = \frac{-jkZ_0}{4\pi} dP_e(Q') T_0 Se^{-jkt} \left[ \frac{\rho_g(Q')}{\rho_g(Q)} \right]^{-1/6} \sqrt{\frac{d\psi_0}{d\psi}} \sqrt{\frac{1}{s(\rho_c+s)}} e^{-jks+0[m^{-2}]} \quad (18)$$

where  $T_0 = T(Q')\rho_g(Q')$  with  $T(Q')$  being the surface torsion at the source location (refer to Table 1).

### C. LIT REGION

From geometrical optics, the source  $d\bar{P}_m(Q')$  at  $Q'$  excites waves which propagate along straight line ray paths from the source to field point in the lit region. As shown in Figure 5, the field  $d\bar{E}_m(P_L)$  at point  $P_L$  is expressed by

$$d\bar{E}_m(P_L) \sim d\bar{E}_m(\tilde{P}_0) \sqrt{\frac{\rho_1^i \rho_2^i}{(\rho_1^i + s_0^i)(\rho_2^i + s_0^i)}} e^{-jk\tilde{s}_0} e^{-0[m_x^{-2}, m_x^{-3}]} \quad (19)$$

Since  $Q'$  is the only caustic of the incident rays, the principal radii of curvature  $\rho_1^i$  and  $\rho_2^i$  associated with the incident wavefront at  $\tilde{P}_0$  are identical, i. e.,  $\rho_1^i = \rho_2^i = \rho_1^i$ . Furthermore,  $d\bar{E}_m(P_L)$  is independent of the reference point  $\tilde{P}_0$ . If  $\tilde{P}_0$  is chosen to be at  $Q'$ , it follows that

$$\lim_{\substack{\tilde{P}_0 \rightarrow Q' \\ \rho_1^i \rightarrow 0 \\ \tilde{s}_0^i \rightarrow s}} \rho_1^i d\bar{E}_m(P_0) = \frac{2}{L_m} \quad (20)$$

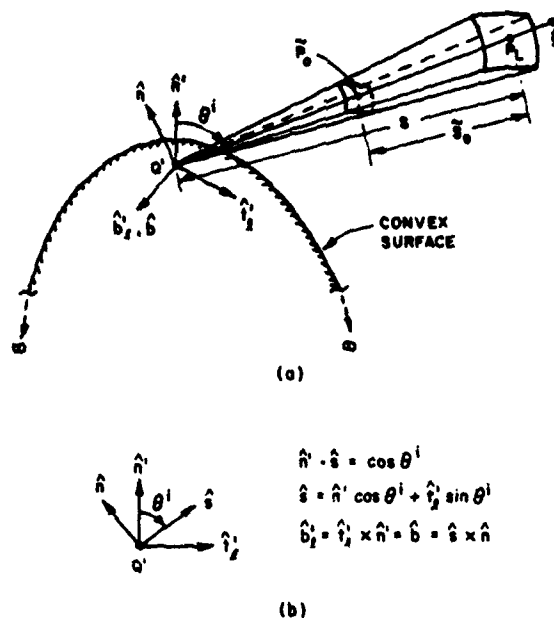


Figure 5. Ray tube and ray coordinates.

should exist. Thus,  $\bar{L}_{\mathbb{Q}}^l$  can be related to  $d\bar{P}_{\mathbb{Q}}(Q')$  by [3]

$$\bar{L}_{\mathbb{Q}}^l = d\bar{P}_{\mathbb{Q}}(Q') \cdot \bar{T}_{\mathbb{Q}}^l \quad (21)$$

Equations (19)-(21) are, then, combined to yield

$$d\bar{E}_{\mathbb{Q}}(P_L) \sim d\bar{P}_{\mathbb{Q}}(Q') \cdot \bar{T}_{\mathbb{Q}}^l \cdot \frac{e^{-jks}}{s} + O[m_L^{-2}, m_L^{-3}, \dots] \quad (22)$$

$$\bar{T}_m^l = \frac{-jk}{4\pi} [\hat{b}_L' \hat{n} A + \hat{t}_L' \hat{b} B + \hat{b}_L' \hat{b} C + \hat{t}_L' \hat{n} D] \quad (23)$$

$$\bar{T}_e^{\ell} = \frac{-jkZ_0}{4\pi} [\hat{n}'\hat{n}M + \hat{n}'\hat{b}N] \quad (24)$$

with A, B, C, D, M, and N are defined in Table 2. Note that  $d\bar{E}_e^m(P_L)$  is decoupled into  $\hat{n}$  and  $\hat{b}$  components as follows:

(a)  $d\bar{P}_m(Q')$  case:

$$dE_m^n(P_L) = \frac{-jk}{4\pi} [(d\bar{P}_m \cdot \hat{b}') (H^\ell + T_0^2 F \cos \theta^\ell) + (d\bar{P}_m \cdot \hat{t}') T_0 F \cos \theta^\ell] \frac{e^{-jks}}{s} + O[m_\ell^{-2}] \quad (25)$$

$$dE_m^b(P_L) = \frac{-jk}{4\pi} [(d\bar{P}_m \cdot \hat{b}') T_0 F + (d\bar{P}_m \cdot \hat{t}') (S^\ell - T_0^2 F \cos^2 \theta^\ell)] \frac{e^{-jks}}{s} + O[m_\ell^{-2}, m_\ell^{-3}] \quad (26)$$

(b)  $d\bar{P}_e(Q')$  case:

$$dE_e^n(P_L) = \frac{-jkZ_0}{4\pi} dP_e(Q') \sin \theta^\ell [H^\ell + T_0^2 F \cos \theta^\ell] \frac{e^{-jks}}{s} + O[m_\ell^{-2}] \quad (27)$$

$$dE_e^b(P_L) = \frac{-jkZ_0}{4\pi} dP_e(Q') \sin \theta^\ell T_0 F \frac{e^{-jks}}{s} + O[m_\ell^{-2}] \quad (28)$$

where

$$H^\ell = g(\epsilon_\ell) e^{-j\epsilon_\ell^3/3} \quad (29)$$

$$S^\ell = \frac{-j}{m_\ell(Q')} \tilde{g}(\epsilon_\ell) e^{-j\epsilon_\ell^3/3} \quad (30)$$

and

$$\epsilon_z = -m_z(Q') \cos \theta^1 \quad (31)$$

$$m_z(Q') = \frac{m(Q')}{(1 + T_0^2 \cos^2 \theta^1)^{1/3}} \quad (32)$$

The angle  $\theta^1$  is defined by  $\hat{n}^1 \cdot \hat{s} = \cos \theta^1$  as shown in Figure 5. Also,

$$F = \frac{S^z - H^z \cos \theta^1}{1 + T_0^2 \cos^2 \theta^1} \quad (33)$$

as defined in Table II.

TABLE II (FOR LIT REGION)

SLOT ON $\phi_0$ CASE				MONOPOLE ON $\phi_0$ CASE		$T_0$	$F$
A	B	C	D	M	N		
$H^z + T_0^2 F \cos \theta^1$	$S^z - T_0^2 F \cos^2 \theta^1$	$T_0 F$	$T_0 F \cos \theta^1$	$\sin \theta^1 [H^z + T_0^2 F \cos \theta^1]$	$\sin \theta^1 T_0 F$	$T(\theta^1) A_0(0^1)$	$\frac{S^z - H^z \cos \theta^1}{1 + T_0^2 \cos^2 \theta^1}$

#### D. PATTERN FACTORS

The solutions for short magnetic or electric dipoles have been given in part (B) and (C). One approach to analyze an extended aperture or linear antenna problem is to integrate the above solutions over the source distribution, if it is known. This is an application of the superposition theorem, and one approximates the source distribution by an array of short magnetic (or electric) dipoles on the conducting surface. This is an accurate solution, however, rather tedious. A more efficient approach is to modify  $d\bar{P}_e^m(Q')$  as shown in Reference 5 such that

(a) in the shadow region:

$$\bar{P}_m = \hat{p}_m \frac{2B}{\pi} \left[ \frac{\cos(\frac{kB}{2}(\hat{p}_m \cdot \hat{t}'))}{1 - (\frac{kB}{\pi}(\hat{p}_m \cdot \hat{t}'))^2} \right] \left[ \frac{\sin(\frac{kA}{2}(\hat{p}_m \cdot \hat{b}'))}{\frac{kA}{2} \hat{p}_m \cdot \hat{b}'} \right]$$

$$\bar{P}_e = \hat{n}' [1 - \cos(kL)] \quad (35)$$

(b) in the lit region:

$$\bar{P}_m = \hat{p}_m \frac{2B}{\pi} \left[ \frac{\cos(\frac{kB}{2} \sin \theta' (\hat{p}_m \cdot \hat{t}'))}{1 - (\frac{kB}{\pi} \sin \theta' (\hat{p}_m \cdot \hat{t}'))^2} \right] \left[ \frac{\sin(\frac{kA}{2} \sin \theta' (\hat{p}_m \cdot \hat{b}'))}{\frac{kA}{2} \sin \theta' (\hat{p}_m \cdot \hat{b}')} \right] \quad (36)$$

$$\bar{P}_e = \hat{n}' \frac{\cos(kL \hat{n}' \cdot \hat{s}) - \cos(kL)}{1 - (\hat{n}' \cdot \hat{s})^2} \quad (37)$$

Here  $\hat{p}_m$  = unit vector in the direction of magnetic current moment,

A, B = the length of the short and long sides of the slot, and

L = the length of the monopole.

It is noted that L is not to exceed a quarter wavelength for the solutions to be valid.

### E. SPHEROID SURFACE PARAMETERS

The formulations in sections (B)-(D) are used to solve for the radiated fields of antennas mounted on a prolate spheroid. Using the spheroid geometry shown in Figure 6, the surface is defined by

$$\vec{R}(\theta, \phi) = R(\theta) \sin \theta \cos \phi \hat{x} + R(\theta) \sin \theta \sin \phi \hat{y} + R(\theta) \cos \theta \hat{z} \quad (38)$$

with

$$R(\theta) = \frac{ac}{\sqrt{a^2 \cos^2 \theta + c^2 \sin^2 \theta}} \quad (39)$$

or,

$$\vec{R}(\nu, \phi) = a \cos \nu \cos \phi \hat{x} + a \cos \nu \sin \phi \hat{y} + c \sin \nu \hat{z} \quad (40)$$

with

$$\tan \nu = \frac{c \cos \theta}{a \sin \theta} \quad (41)$$

The " $\nu$ " parameter is introduced because of its convenience in analyzing elliptic geometries.

Considering a ray which propagates along a geodesic path  $Q'Q$  on the spheroidal surface as shown in Figure 7, the three unit vectors  $\hat{t}$ ,  $\hat{n}$  and  $\hat{b}$  are, as defined earlier, the geodesic tangent, outward surface normal and binormal at any point along the geodesic path. The outward surface unit normal ( $\hat{n}$ ) is obtained from

$$\hat{n} = \frac{\vec{R}_\phi \times \vec{R}_\nu}{|\vec{R}_\phi \times \vec{R}_\nu|} \quad (42)$$

where

$$\frac{\partial \vec{R}}{\partial \nu} = \vec{R}_\nu = -a \sin \nu \cos \phi \hat{x} - a \sin \nu \sin \phi \hat{y} + c \cos \nu \hat{z}$$

and

$$\frac{\partial \vec{R}}{\partial \phi} = \vec{R}_\phi = -a \cos \nu \sin \phi \hat{x} + a \cos \nu \cos \phi \hat{y} \quad .$$

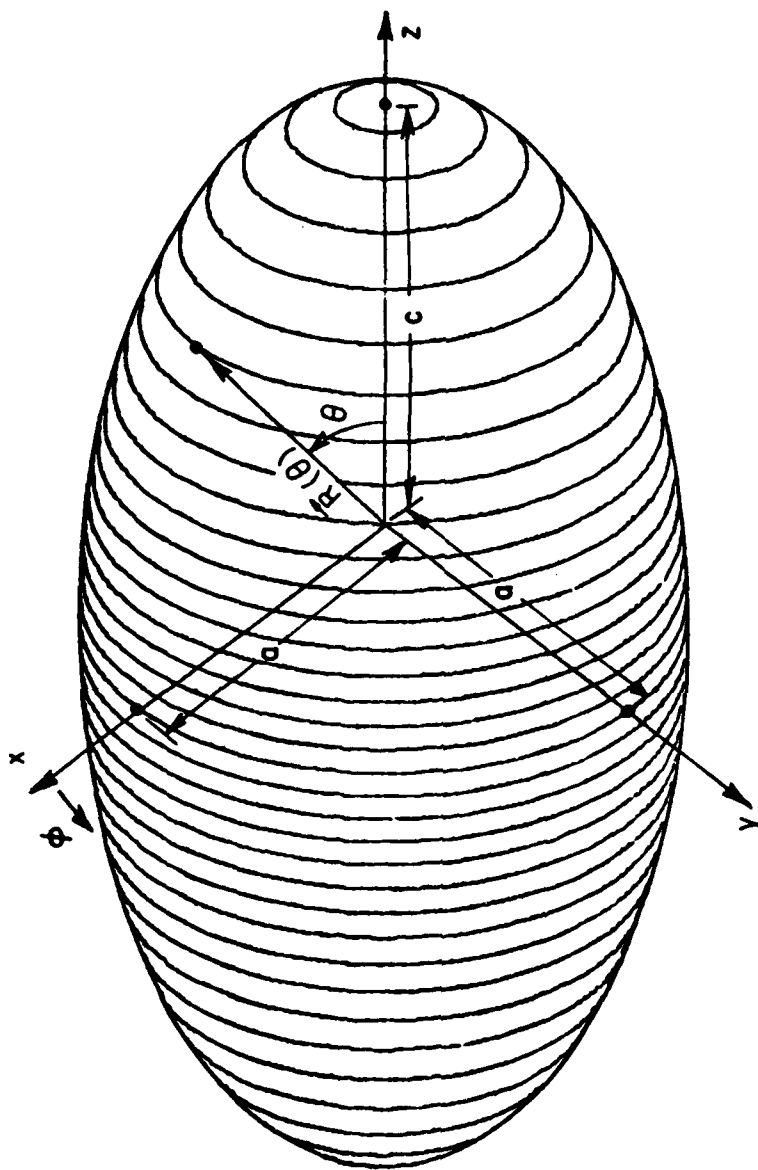


Figure 6. Geometry of a spheroid.



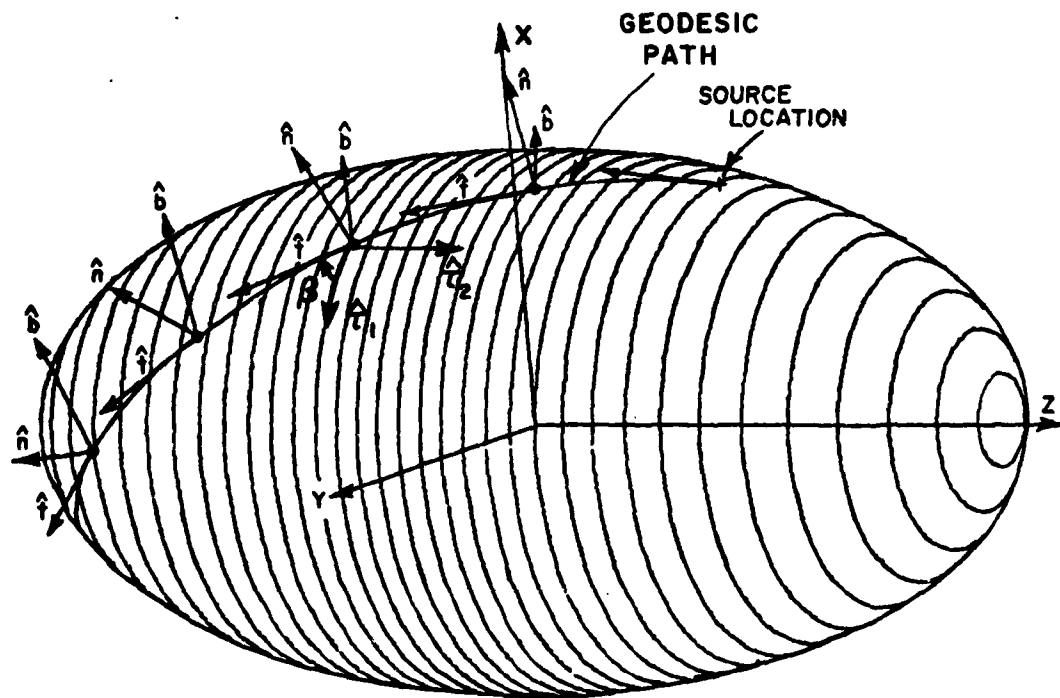


Figure 7. Geodesic path on a spheroid.

Then,

$$\hat{n} = \frac{c \cos v \cos \phi \hat{x} + c \cos v \sin \phi \hat{y} + a \sin v \hat{z}}{\sqrt{a^2 \sin^2 v + c^2 \cos^2 v}} \quad (43)$$

The normal curvatures  $\kappa_n$  on the surface are evaluated by introducing the first and second fundamental forms of differential geometry [4] such that

$$\kappa_n = \frac{L d\phi^2 + 2M d\phi dv + N dv^2}{E d\phi^2 + 2F d\phi dv + G dv^2} \quad (44)$$

where

$$L = \vec{R}_{\phi\phi} \cdot \vec{N}, \quad M = \vec{R}_{\phi v} \cdot \vec{N}, \quad N = \vec{R}_{vv} \cdot \vec{N}$$

$$E = \vec{R}_{\phi} \cdot \vec{R}_{\phi}, \quad F = \vec{R}_{\phi} \cdot \vec{R}_v, \quad G = \vec{R}_v \cdot \vec{R}_v$$

and

$$\vec{N} = -\hat{n}.$$

It can be shown that

$$\vec{R}_{\phi\phi} = -a \cos v \cos \phi \hat{x} - a \cos v \sin \phi \hat{y},$$

$$\vec{R}_{\phi v} = a \sin v \sin \phi \hat{x} - a \sin v \cos \phi \hat{y}, \text{ and}$$

$$\vec{R}_{vv} = -a \cos v \cos \phi \hat{x} - a \cos v \sin \phi \hat{y} - c \sin v \hat{z}.$$

After some algebraic manipulation, one obtains

$$L = ac \cos^2 v / \sqrt{a^2 \sin^2 v + c^2 \cos^2 v}$$

$$M = 0$$

$$N = ac/\sqrt{a^2 \sin^2 v + c^2 \cos^2 v}$$

$$E = a^2 \cos^2 v$$

$$F = 0$$

$$G = a^2 \sin^2 v + c^2 \cos^2 v$$

The two principal curvatures on the surface are, then, given by

$$\kappa_1 = L/E = \frac{c}{a \sqrt{a^2 \sin^2 v + c^2 \cos^2 v}} \quad (45)$$

and

$$\kappa_2 = N/G = \frac{ac}{(a^2 \sin^2 v + c^2 \cos^2 v)^{3/2}} \quad (46)$$

which can, also, be expressed as

$$\kappa_1 = \frac{c}{a} \sqrt{\frac{a^2 \cos^2 \theta + c^2 \sin^2 \theta}{a^4 \cos^2 \theta + c^4 \sin^2 \theta}} \quad (47)$$

and

$$\kappa_2 = \frac{ac(a^2 \cos^2 \theta + c^2 \sin^2 \theta)^{3/2}}{(a^4 \cos^2 \theta + c^4 \sin^2 \theta)^{3/2}} \quad (48)$$

It is noticed that  $R_1 = \frac{1}{\kappa_1}$  and  $R_2 = \frac{1}{\kappa_2}$  as found in Table I. Since  $F=M=0$ , the directions  $\vec{R}_\phi$  and  $\vec{R}_v$  are in the principal surface directions [4] which are expressed by  $\hat{\tau}_1, \hat{\tau}_2$  and are associated with  $\kappa_1$  and  $\kappa_2$ , respectively, as shown in Figure 7. If  $\beta$  denotes the angle between  $\hat{t}$  and  $\hat{\tau}_1$ , then

$$\hat{t} = \hat{\tau}_1 \cos \beta + \hat{\tau}_2 \sin \beta \quad (49)$$

From Euler's theorem, the normal curvature along the geodesic path is specified by

$$\kappa_g = \kappa_1 \cos^2 \beta + \kappa_2 \sin^2 \beta \quad (50)$$

with the radius of curvature ( $\rho_g$ ) being  $1/\kappa_g$ .

The torsion term ( $T_g$ ) introduced in Section (B) is given by

$$T_g = T \cdot \rho_g \quad (51)$$

where the surface torsion is given by

$$T = \frac{\sin 2\beta}{2} (\kappa_2 - \kappa_1) \quad (52)$$

with  $\kappa_1$  and  $\kappa_2$  being defined in Equations (45)-(48).

## CHAPTER III

### NUMERICAL TECHNIQUE AND PERTURBATION METHOD

#### A. INTRODUCTION

It is seen that, for an antenna mounted on a spheroid, the solution in the lit region is relatively straightforward. On the other hand, the geodesic paths associated with the GTD solution in the shadow region are extremely complex. Previous studies [2] employed calculus of variations or tensor analysis to calculate the geodesic paths which resulted in very inefficient solutions. An efficient numerical approach is examined in this chapter with the spheroid simulated by a perturbed cone or cylinder model. In that the cone and cylinder are developed surfaces, geodesics are, then efficient to solve. Given a radiation direction  $(\theta_t, \phi_t)$ , one can find the final diffraction point  $(\theta_Q, \phi_Q)$  by following the geodesic path, step by step, until the geodesic tangent coincides with  $(\theta_t, \phi_t)$ . This is a rather tedious and time consuming process if applied for each new radiation direction. Considering a new radiation direction does not deviate greatly from the previous direction, one should be able to develop a solution which uses the properties of the surface and the previous geodesic path to find the new diffraction point. Such an approach is applied here to make this solution as efficient as possible.

Since the field decays exponentially along the ray path on the surface, it is assumed that only one or possibly two dominant rays exist in the problems treated.

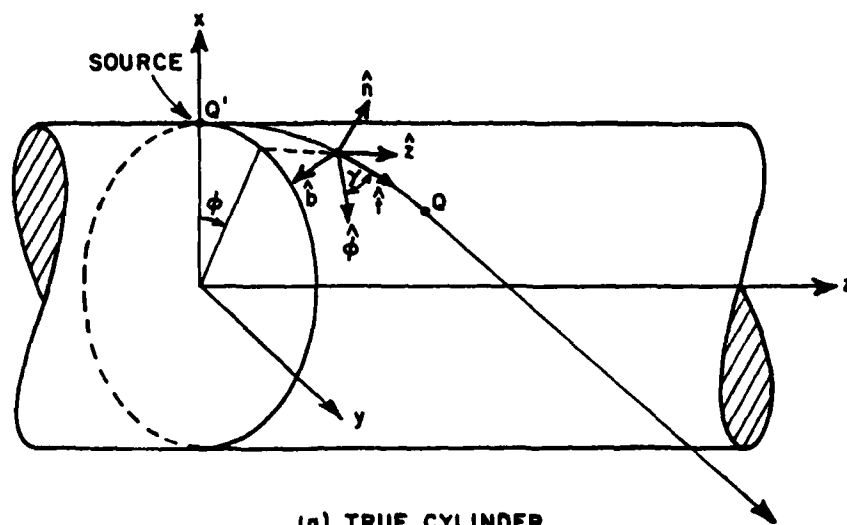
#### B. SURFACE GEODESICS

The geodesics on the cylinder, cone and spheroid are examined in this section.

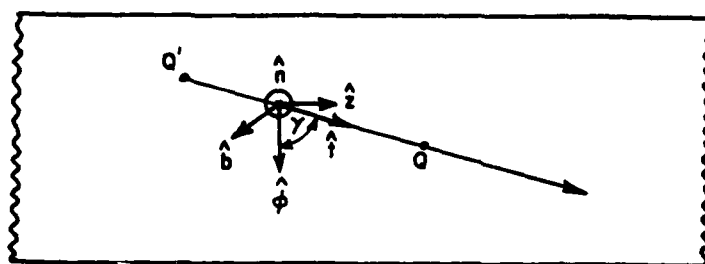
##### (a) Cylinder case:

The circular cylinder geometry used for this study is shown in Figure 8(a). Since the cylinder is a developed surface, the geodesic path  $Q'Q$  is a straight line on the unfolded planar surface. As shown in Figure 8(b), the geodesic unit tangent  $\hat{t}$  is given by

$$\hat{t} = \hat{\phi} \cos \gamma + \hat{z} \sin \gamma \quad (53)$$



(a) TRUE CYLINDER



(b) UNFOLDED PLANAR SURFACE

Figure 8. Geodesic path on a developed cylinder.

where

$$\hat{\phi} = -\sin\phi\hat{x} + \cos\phi\hat{y}. \quad (54)$$

It is noticed that  $\hat{\phi}$  and  $\hat{z}$  are the two principal directions on the cylinder surface. For a given geodesic Q'Q, one can see that  $\gamma$  is a constant along the geodesic path.

(b) Cone case:

Consider a ray propagates along a geodesic path Q'Q on the cone surface as shown in Figure 9(a) which is a straight line on the unfolded planar surface as shown in Figure 9(b) since the cone is a developed surface. Applying the same technique as in Section II-(E),  $\hat{t}_e$  and  $\hat{\phi}$  are the two principal directions on the surface. The geodesic unit tangent  $\hat{t}$  is, then, represented by

$$\hat{t} = \hat{\phi}\cos\beta + \hat{t}_e\sin\beta \quad (55)$$

where

$$\hat{t}_e = -\hat{x}_e\sin\delta + \hat{z}\cos\delta, \quad (56)$$

$$\hat{x}_e = \cos\phi\hat{x} + \sin\phi\hat{y}, \quad (57)$$

and  $\delta$  is the half cone angle as shown in Figure 9(a). Note that  $\beta$  is no longer a constant along the geodesic path Q'Q.

(c) Spheroid case:

Recall that the prolate spheroid surface is defined by

$$\tilde{R}(\nu, \phi) = a \cos\nu\cos\phi\hat{x} + a \cos\nu\sin\phi\hat{y} + c \sin\nu\hat{z}$$

with

$$\tan\nu = \frac{c \cos\theta}{a \sin\theta}.$$

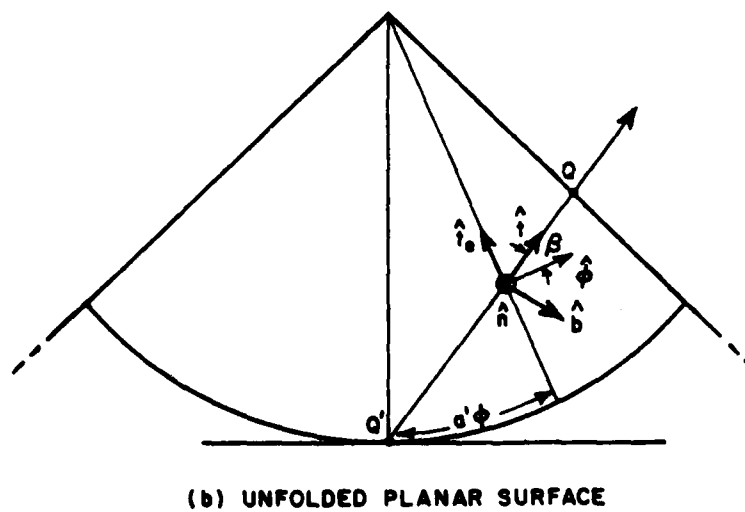
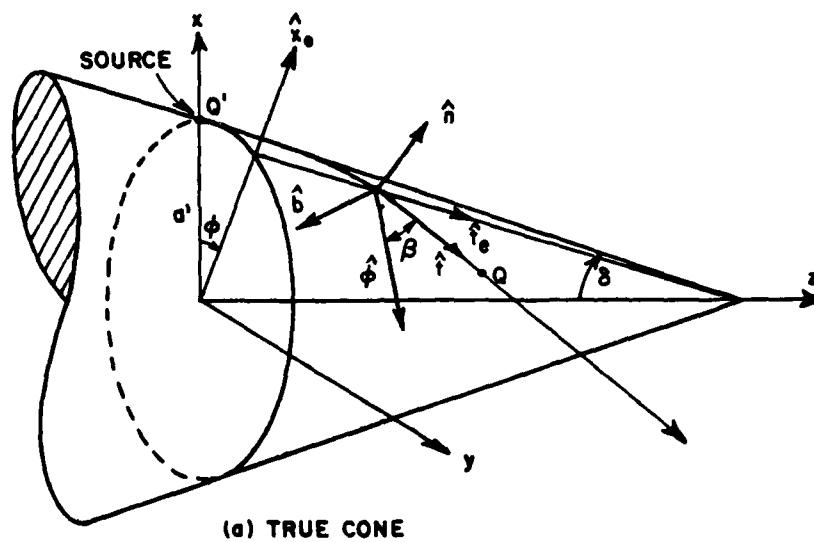


Figure 9. Geodesic path on a developed cone.





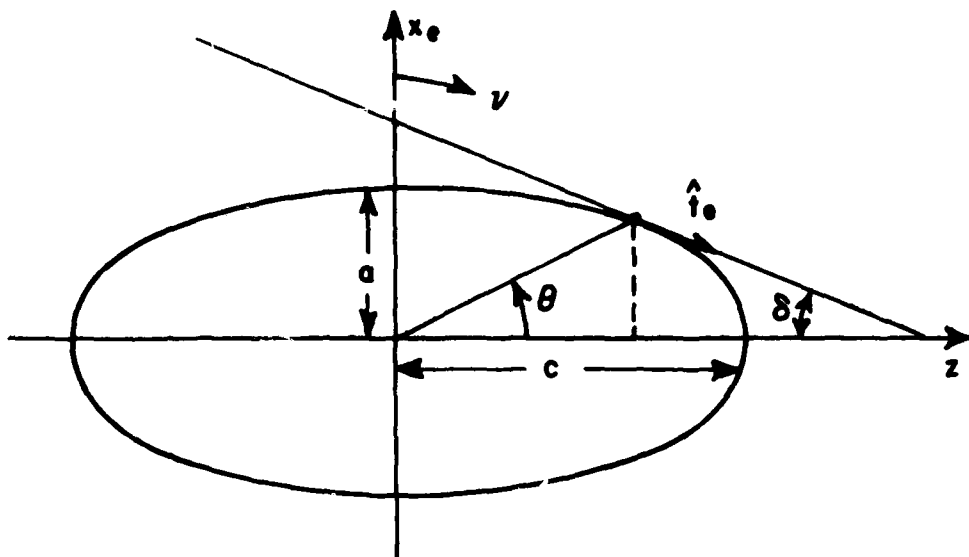


Figure 10(b). Elliptic profile

From Section II-(E), it was found that the principal directions were given by  $\vec{R}_\phi$  and  $\vec{R}_v$ . As seen in Figure 10(a) and (b) the unit vectors in the principal directions can be represented by

$$\hat{t}_r = \vec{R}_\phi / |\vec{R}_\phi| = -\hat{x} \sin \phi + \hat{y} \cos \phi \quad (58)$$

$$\begin{aligned} \hat{t}_e &= \vec{R}_v / |\vec{R}_v| = -\hat{x}_e \sin \delta + \hat{z} \cos \delta \\ &= \frac{-a \sin v \hat{x}_e + c \cos v \hat{z}}{\sqrt{a^2 \sin^2 v + c^2 \cos^2 v}} \end{aligned} \quad (59)$$

with

$$\hat{x}_e = \cos \phi \hat{x} + \sin \phi \hat{y} \quad (60)$$

It is noticed that  $\hat{t}_r$  is merely  $\hat{\phi}$ . If  $\beta$  denotes the angle between  $\hat{t}_r$  and the geodesic unit tangent  $\hat{t}$ , then

$$\hat{t} = \hat{t}_r \cos \beta + \hat{t}_e \sin \beta, \quad (61)$$

which is identical to the form used for the cylinder and cone geodesics. This suggests that one might be able to develop a perturbation solution which gives a simplified form for  $\beta$  on a spheroid using the cylinder or cone expressions for  $\beta$ .

### C. CYLINDER PERTURBATION

In order to solve for the geodesics on a prolate spheroid, the cylinder perturbation technique is used when the source is located at  $\theta_s = 90^\circ$ . As shown in Figure 11, the cylinder is perturbed by bending it around the spheroid, and the geodesics are to be resolved on this perturbed cylinder model. Note that the source position is assumed to be in the  $\phi_s = 0$  plane, in that different  $\phi_s$  locations can be dealt with by simply rotating the pattern axes.

Recalling that  $\gamma$  is a constant along a given geodesic path Q'Q on the perturbed cylinder in Figure 11, one obtains a geodesic equation given by

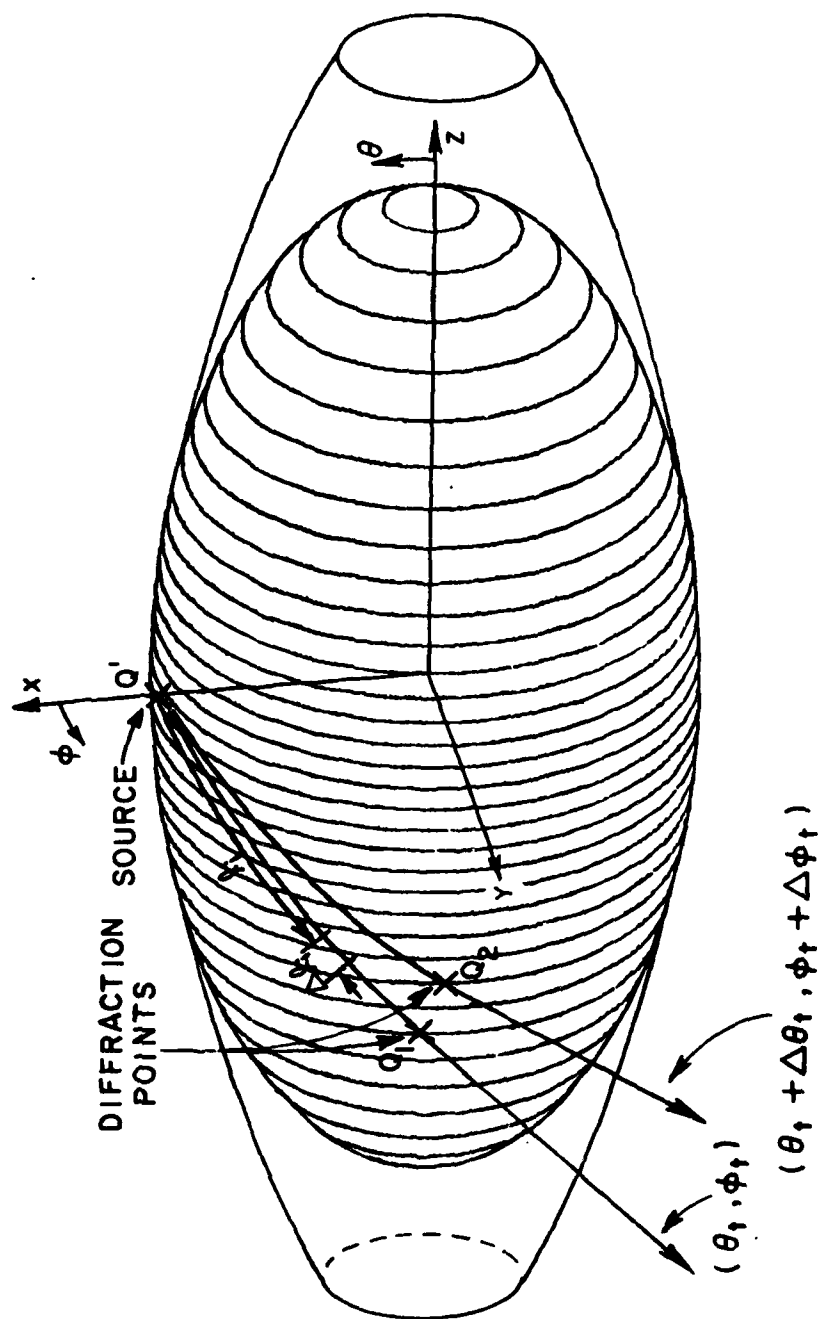


Figure 11. Cylinder perturbation.

$$\tan \gamma = \frac{S_e}{S_r} \quad (62)$$

with  $S_r = a\phi$ . The elliptic cross-section in the  $x_e$ - $z$  plane is described by

$$x_e = a \cos v'$$

$$z = c \sin v'$$

therefore,

$$\begin{aligned} s_e &= \int_0^v \sqrt{\left(\frac{dx_e}{dv'}\right)^2 + \left(\frac{dz}{dv'}\right)^2} dv' \\ &= \int_0^v \sqrt{a^2 \sin^2 v' + c^2 \cos^2 v'} dv' \end{aligned}$$

Thus, Equation (62) becomes

$$\tan \gamma = \frac{\int_0^v \sqrt{a^2 \sin^2 v' + c^2 \cos^2 v'} dv'}{a\phi} \quad (63)$$

with  $-\pi \leq \gamma \leq \pi$ , and  $-\frac{\pi}{2} \leq \phi, v' \leq \frac{\pi}{2}$ . At the diffraction point Q, the radiation direction  $(\theta_t, \phi_t)$  should coincide with the geodesic tangent  $\hat{t}$  given in Equation (61). Thus,

$$\begin{aligned} \hat{t} &= \hat{x} \sin \theta_t \cos \phi_t + \hat{y} \sin \theta_t \sin \phi_t + \hat{z} \cos \theta_t \\ &= \hat{t}_r \cos \gamma + \hat{t}_e \sin \gamma \end{aligned} \quad (64)$$

Equating the x-, y-, and z-components respectively, one obtains

$$t_x : -\sin\phi\cos\gamma - \frac{a \sin\gamma\cos\phi\sin\gamma}{\sqrt{a^2\sin^2\gamma + c^2\cos^2\gamma}} = \sin\theta_t\cos\phi_t \quad (65)$$

$$t_y : \cos\phi\cos\gamma - \frac{a \sin\gamma\sin\phi\sin\gamma}{\sqrt{a^2\sin^2\gamma + c^2\cos^2\gamma}} = \sin\theta_t\sin\phi_t \quad (66)$$

$$t_z : \frac{c \cos\gamma\sin\gamma}{\sqrt{a^2\sin^2\gamma + c^2\cos^2\gamma}} = \cos\theta_t \quad (67)$$

Now,  $t_y\cos\phi - t_x\sin\phi$  yields

$$\cos\gamma = \sin\theta_t\sin(\phi_t - \phi) \quad (68)$$

Equation (67) is divided by (68) to give

$$\frac{c \cos\gamma\sin\gamma}{\sqrt{a^2\sin^2\gamma + c^2\cos^2\gamma}} = \frac{\cot\theta_t}{\sin(\phi_t - \phi)}$$

By combining Equation (63) with the above expression, one obtains the following:

$$\begin{aligned} f(\theta_t, \phi_t, \gamma, \phi) &= c \cos\gamma\sin(\phi_t - \phi) \int_0^\gamma \sqrt{a^2\sin^2\gamma' + c^2\cos^2\gamma'} d\gamma' \\ &\quad - a\phi\cot\theta_t \cdot \sqrt{a^2\sin^2\gamma + c^2\cos^2\gamma} \\ &= 0 \end{aligned} \quad (69)$$

Next, Equations (67) and (68) are squared, which gives

$$c^2 \cos^2 \nu \sin^2 \gamma = \cos^2 \theta_t (a^2 \sin^2 \nu + c^2 \cos^2 \nu)$$

$$\cos^2 \gamma = \sin^2 \theta_t \sin^2 (\phi_t - \phi)$$

From the above two expressions, one obtains

$$c^2 \cos^2 \nu = \cos^2 \theta_t (a^2 \sin^2 \nu + c^2 \cos^2 \nu) + c^2 \cos^2 \nu \sin^2 \theta_t \sin^2 (\phi_t - \phi) .$$

Another function is, then, defined by

$$g(\theta_t, \phi_t, \nu, \phi) = \cos^2 \theta_t (a^2 \sin^2 \nu + c^2 \cos^2 \nu) + c^2 \cos^2 \nu \sin^2 \theta_t \sin^2 (\phi_t - \phi) - c^2 \cos^2 \nu = 0. \quad (70)$$

Provided that one has obtained a diffraction point  $(\nu, \phi)$  for a radiation direction  $(\theta_t, \phi_t)$ , a numerical technique can now be developed from Equations (69) and (70) to solve for  $(\nu + \Delta \nu, \phi + \Delta \phi)$  associated with a new radiation direction  $(\theta_t + \Delta \theta_t, \phi_t + \Delta \phi_t)$ . Assuming that the  $i$ th set of  $(\theta_t, \phi_t, \nu, \phi)$  is first known to satisfy  $f_i = g_i = 0$ , or at least approximately so, the next set  $(\theta_t + \Delta \theta_t, \phi_t + \Delta \phi_t, \nu + \Delta \nu, \phi + \Delta \phi)$  is obtained by enforcing  $f_{i+1} = g_{i+1} = 0$ , such that

$$f_{i+1} = f_i + f_{\theta_t} \Delta \theta_t + f_{\phi_t} \Delta \phi_t + f_{\nu} \Delta \nu + f_{\phi} \Delta \phi = 0, \text{ and}$$

$$g_{i+1} = g_i + g_{\theta_t} \Delta \theta_t + g_{\phi_t} \Delta \phi_t + g_{\nu} \Delta \nu + g_{\phi} \Delta \phi = 0.$$

In matrix form, it is given by

$$\begin{bmatrix} f_v & f_\phi \\ g_v & g_\phi \end{bmatrix} \begin{bmatrix} \Delta v \\ \Delta \phi \end{bmatrix} = \begin{bmatrix} -f_i - f_{\theta_t} \Delta \theta_t - f_{\phi_t} \Delta \phi_t \\ -g_i - g_{\theta_t} \Delta \theta_t - g_{\phi_t} \Delta \phi_t \end{bmatrix} \quad (71)$$

Note that the partial derivatives are given by the following:

$$\begin{aligned} f_v &= c \sin(\phi_t - \phi) \left[ -\sin v \int_0^v \sqrt{a^2 \sin^2 v' + c^2 \cos^2 v'} dv' \right. \\ &\quad \left. + \cos v \cdot \sqrt{a^2 \sin^2 v + c^2 \cos^2 v} \right] \\ &\quad + \frac{a\phi}{2} (c^2 - a^2) \sin 2v \cdot \cot \theta_t / \sqrt{a^2 \sin^2 v + c^2 \cos^2 v} \end{aligned}$$

$$\begin{aligned} f_\phi &= -c \cos v \cos(\phi_t - \phi) \int_0^v \sqrt{a^2 \sin^2 v' + c^2 \cos^2 v'} dv' \\ &\quad - a \sqrt{a^2 \sin^2 v + c^2 \cos^2 v} \cdot \cot \theta_t \end{aligned}$$

$$f_{\theta_t} = a\phi \csc \theta_t \cdot \sqrt{a^2 \sin^2 v + c^2 \cos^2 v}$$

$$f_{\phi_t} = c \cos v \cos(\phi_t - \phi) \int_0^v \sqrt{a^2 \sin^2 v' + c^2 \cos^2 v'} dv'$$

$$g_v = \sin 2v \cdot [a^2 \cos^2 \theta_t + c^2 \sin^2 \theta_t \cos^2(\phi_t - \phi)]$$

$$g_\phi = -c^2 \cos^2 v \sin^2 \theta_t \sin^2(\phi_t - \phi)$$

$$g_{\theta_t} = -\sin 2\theta_t [a^2 \sin^2 v + c^2 \cos^2 v \cos^2(\phi_t - \phi)]$$

$$g_{\phi_t} = c^2 \cos^2 v \sin^2 \theta_t \sin^2(\phi_t - \phi)$$

Therefore, one obtains  $(\Delta v, \Delta \phi)$  for a known  $(\Delta \theta_t, \Delta \phi_t)$ , using



Equation (71). In order to determine the initial diffraction point  $(\nu, \phi)$  for a radiation direction  $(\theta_t, \phi_t)$ , one can always assume a diffraction point at the source  $(\nu, \phi) = (0, 0)$  with the radiation direction  $(\theta_t, \pm \frac{\pi}{2})$ , and gradually add increments  $(\Delta\theta_t, \Delta\phi_t)$  until the desired radiation direction  $(\theta_t, \phi_t)$  is reached. After the initial diffraction point is identified by  $(\nu, \phi)$ ;  $\gamma$ , and therefore, the geodesic path is determined by Equation (63). Such a numerical approach is illustrated in Figure 11. Note that one need not trace out the complete geodesic path from the source location to the diffraction point for each new radiation direction. As shown in Figure 11, the diffraction point  $(\nu + \Delta\nu, \phi + \Delta\phi)$  for the next radiation direction is determined from  $(\nu, \phi)$ , using Equation (71), if  $(\Delta\theta_t, \Delta\phi_t)$  are small which is the case when a complete radiation pattern is computed.

After the geodesic path is determined, various other parameters associated with Equations (15)-(18) must be found. The Fock parameter  $\xi$  of Equation (12) is given by

$$\xi = \int_0^Q \frac{1}{Q' \rho_g} \left( \frac{k_{\rho g}}{2} \right)^{1/3} d\ell, \quad ,$$

where the integral is evaluated along the geodesic path. Note that  $\ell$  is the arc length along the geodesic and given by

$$\ell = \frac{S_e}{\sin \gamma} = \frac{S_r}{\cos \gamma} \quad .$$

Therefore,

$$d\ell = \frac{1}{\sin \gamma} \sqrt{a^2 \sin^2 \nu + c^2 \cos^2 \nu} d\nu$$

or,

$$d\ell = \frac{1}{\cos \gamma} a d\phi \quad ,$$

and the integration can be rewritten as

$$\xi = \frac{1}{\sin \gamma} \int_0^\psi \frac{1}{\rho_g} \left( \frac{k \rho_g}{2} \right)^{1/3} \cdot \sqrt{a^2 \sin^2 \psi' + c^2 \cos^2 \psi'} d\psi' \quad (72)$$

or

$$\xi = \frac{a}{\cos \gamma} \int_0^\phi \frac{1}{\rho_g} \left( \frac{k \rho_g}{2} \right)^{1/3} d\phi' \quad (73)$$

where  $\rho_g = 1/(\kappa_1 \cos^2 \gamma + \kappa_2 \sin^2 \gamma)$ , and  $\kappa_1, \kappa_2$  are given in Equations (45) and (46).

Next, the ray divergence factor  $\sqrt{\frac{d\psi_0(Q')}{d\psi(Q)}}$  is defined as the change in the separation of adjacent surface rays, and it can be found from a numerical approach by setting  $\ell = \text{constant}$ . The ray geometry is shown in Figure 12.

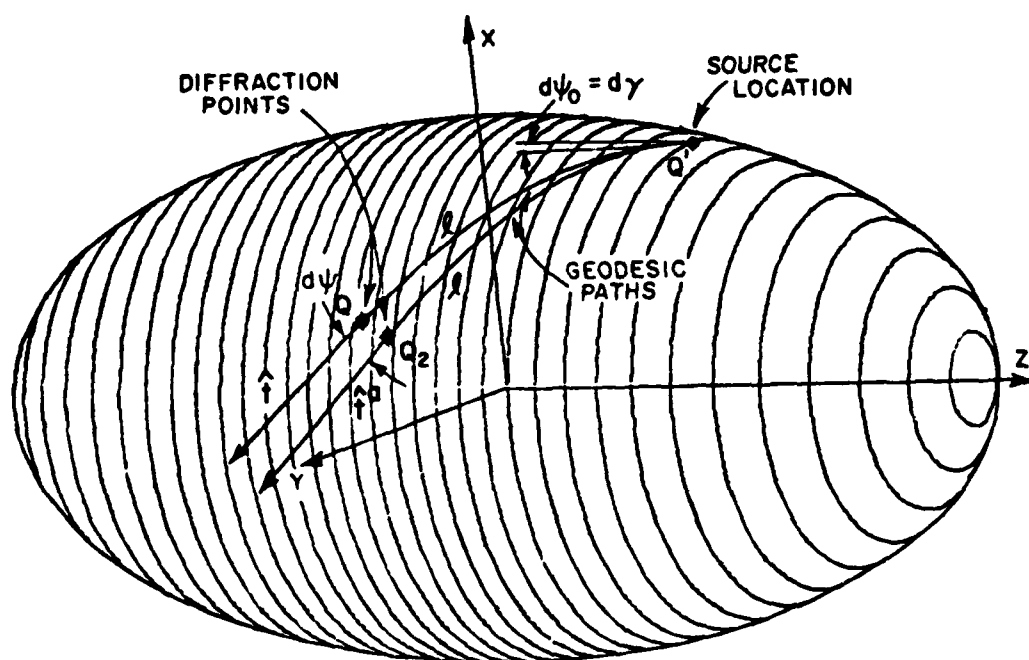


Figure 12. Illustration of the spread factor  $(\sqrt{d\psi_0/d\psi})$  terms.

Now, Equation (62) is rewritten as

$$\frac{S_r}{\sqrt{k^2 - S_r^2}} = \cot \gamma$$

therefore,

$$\frac{k^2}{(k^2 - S_r^2)^{3/2}} dS_r = -\csc^2 \gamma d\gamma$$

or

$$\frac{k^2}{S_e^3} a d\phi = -\csc^2 \gamma d\gamma$$

For a known  $d\gamma = d\psi_0$ , usually set equal to  $1^\circ$ ,  $d\phi$  can, then, be determined. Also,

$$\tan(\gamma + d\gamma) = \frac{S_e + \sqrt{a^2 \sin^2 \gamma + c^2 \cos^2 \gamma} dv}{S_r + a d\phi} \quad (74)$$

The diffraction point  $(v + dv, \phi + d\phi)$  of the adjacent ray is, then, obtained from the above equation. The radiation direction of the adjacent ray is given by

$$\hat{t}^a = \hat{t}_r^a \cos(\gamma + d\gamma) + \hat{t}_e^a \sin(\gamma + d\gamma)$$

Recalling that the original radiation direction is

$$\hat{t} = \hat{t}_r \cos \gamma + \hat{t}_e \sin \gamma$$

then one obtains

$$\cos(d\psi) = \hat{t} \cdot \hat{t}^a. \quad (75)$$

In other words,

$$\sqrt{\frac{d\psi_o(Q')}{d\psi(Q)}} = \sqrt{\frac{dy}{\cos^{-1}(\hat{t} \cdot \hat{t}^a)}}$$

where  $dy$  can be conveniently chosen as  $1^\circ$ .

This completes the cylinder perturbation solution, which is applied if the antenna is mounted on the mid-section of the prolate spheroid ( $\theta_s = 90^\circ$ , in Figure 1).

#### D. CONE PERTURBATION

When the source is not located at the mid-section ( $\theta_s \neq 90^\circ$ , in Figure 14), the cone perturbation model is used. As shown in Figure 13(a), the spheroid is modeled by a perturbed cone. The associated unfolded surface is shown in Figure 13(b). If  $\gamma$  and  $\beta$  denote the angle between  $\hat{t}$  and  $\hat{t}_r$  at  $Q'$  and  $Q$  respectively, it is seen in Section III-(B) that they are not the same as in the cylinder case. In fact,

$$\beta = \gamma - \alpha \quad (76)$$

where

$$\alpha = \frac{S_r}{r} = \frac{a' \phi}{r}$$

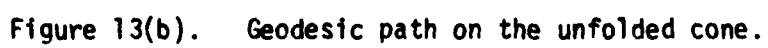
with  $a' = a \cos \nu_s$  and  $\tan \nu_s = \frac{a \cos \theta_s}{c \sin \theta_s}$ . With some manipulation, one can show that

$$(r - S_e) \cos(\gamma - \alpha) = r \cos \gamma \quad (77)$$

where

$$S_e = \int_{\nu_s}^{\nu} \sqrt{a^2 \sin^2 \nu' + c^2 \cos^2 \nu'} d\nu'.$$





At the diffraction point  $(\nu, \phi)$ , the radiation direction  $(\theta_t, \phi_t)$  coincides with the geodesic tangent  $\hat{t}$ , and one obtains

$$t_x : -\sin\phi\cos(\gamma-\alpha) - \frac{a \sin\nu\cos\phi\sin(\gamma-\alpha)}{\sqrt{a^2\sin^2\nu+c^2\cos^2\nu}} = \sin\theta_t\cos\phi_t$$

$$t_y : \cos\phi\cos(\gamma-\alpha) - \frac{a \sin\nu\sin\phi\sin(\gamma-\alpha)}{\sqrt{a^2\sin^2\nu+c^2\cos^2\nu}} = \sin\theta_t\sin\phi_t$$

$$t_z : \frac{c \cos\nu\sin(\gamma-\alpha)}{\sqrt{a^2\sin^2\nu+c^2\cos^2\nu}} = \cos\theta_t$$

Now,  $t_y\cos\phi - t_x\sin\phi$  yields

$$\cos(\gamma-\alpha) = \sin\theta_t\sin(\phi_t-\phi) \quad (78)$$

Using  $(t_x\cos\phi + t_y\sin\phi)/t_z$  gives

$$-\frac{a}{c}\tan\nu = \tan\theta_t\cos(\phi_t-\phi) \quad (79)$$

Three functions can, then, be constructed as follows from Equations (77)-(79):

$$f(\nu, \alpha, \gamma) = (r-S_e)\cos(\gamma-\alpha) - r\cos\gamma = 0 \quad (80)$$

$$g(\theta_t, \phi_t, \alpha, \gamma) = \cos(\gamma-\alpha) - \sin\theta_t\sin(\phi_t - \frac{r}{a}\alpha) = 0 \quad (81)$$

$$h(\theta_t, \phi_t, \nu, \alpha) = a \cos\theta_t\sin\nu + c \sin\theta_t\cos\nu \cos(\phi_t - \frac{r}{a}\alpha) \quad (82)$$

Using the increment method again, one uses

$$f_{i+1} = f_i + f_v \Delta v + f_\alpha \Delta \alpha + f_\gamma \Delta \gamma = 0 \quad ,$$

$$g_{i+1} = g_i + g_{\theta_t} \Delta \theta_t + g_{\phi_t} \Delta \phi_t + g_\alpha \Delta \alpha + g_\gamma \Delta \gamma = 0 \quad , \text{ and}$$

$$h_{i+1} = h_i + h_{\theta_t} \Delta \theta_t + h_{\phi_t} \Delta \phi_t + h_v \Delta v + h_\alpha \Delta \alpha = 0 \quad .$$

In matrix form, it is given by

$$\begin{bmatrix} f_v & f_\alpha & f_\gamma \\ 0 & g_\alpha & g_\gamma \\ h_v & h_\alpha & 0 \end{bmatrix} \begin{bmatrix} \Delta v \\ \Delta \alpha \\ \Delta \gamma \end{bmatrix} = \begin{bmatrix} -f_i \\ -g_i - g_{\theta_t} \Delta \theta_t - g_{\phi_t} \Delta \phi_t \\ -h_i - h_{\theta_t} \Delta \theta_t - h_{\phi_t} \Delta \phi_t \end{bmatrix} \quad , \quad (83)$$

where the partial derivatives are evaluated using the last radiation direction results  $(\theta_t, \phi_t, v, \phi)$  and are given as follows:

$$f_v = -\sqrt{a^2 \sin^2 v + c^2 \cos^2 v} \cos(\gamma - \alpha)$$

$$f_\alpha = (r - S_e) \sin(\gamma - \alpha)$$

$$f_\gamma = -(r - S_e) \sin(\gamma - \alpha) + r \sin \gamma$$

$$g_\alpha = \sin(\gamma - \alpha) + \frac{r}{a} \sin \theta_t \cos(\phi_t - \frac{r}{a} \alpha)$$

$$g_\gamma = -\sin(\gamma - \alpha)$$

$$g_{\theta_t} = -\cos \theta_t \sin(\phi_t - \frac{r}{a} \alpha)$$

$$g_{\phi_t} = -\sin \theta_t \cos(\phi_t - \frac{r}{a} \alpha)$$

$$h_v = a \cos \theta_t \cos v - c \sin \theta_t \sin v \cos(\phi_t - \frac{r}{a} \alpha)$$



$$h_{\alpha} = c \frac{r}{a} \sin \theta_t \cos \nu \sin(\phi_t - \frac{r}{a} \alpha)$$

$$h_{\theta_t} = -a \sin \theta_t \sin \nu + c \cos \theta_t \cos \nu \cos(\phi_t - \frac{r}{a} \alpha)$$

$$h_{\phi_t} = -c \sin \theta \cos \nu \sin(\phi_t - \frac{r}{a} \alpha) \quad .$$

It is seen that one can solve for  $(\Delta \nu, \Delta \alpha, \Delta \gamma)$ , for a known  $(\Delta \theta_t, \Delta \phi_t)$ , using Equation (83). To obtain a diffraction point  $(\nu, \phi)$  for a radiation direction  $(\theta_t, \phi_t)$ , one can always assume the first diffraction point is at the source  $(\nu, \phi) = (\nu_s, 0)$  with the radiation direction  $(\frac{\pi}{2}, \pm \frac{\pi}{2})$ , and gradually add the increments  $(\Delta \theta_t, \Delta \phi_t)$  until the final radiation direction  $(\theta_t, \phi_t)$  is reached. Again, one need not start out from the source everytime, but obtains the new solution directly from Equation (83), provided that the new radiation direction does not deviate greatly from the previous direction.

The geodesic arc length is obtained from either of the following equations:

$$\begin{aligned} \ell \cos \gamma &= (r - S_e) \sin \alpha \quad , \text{ or} \\ \ell \sin \gamma &= r - (r - S_e) \cos \alpha \quad . \end{aligned} \tag{84}$$

Therefore,

$$\begin{aligned} d\ell &= \frac{r \cos \gamma}{\cos^2(\gamma - \alpha)} d\alpha \quad , \text{ or} \\ d\ell &= \frac{\sqrt{a^2 \sin^2 \nu + c^2 \cos^2 \nu}}{\sin(\gamma - \alpha)} d\nu \end{aligned}$$

and the Fock parameter  $\xi$  is obtained by integrating along  $\nu$  or  $\alpha$ , i.e.,

$$\xi = r \cos \gamma \int_0^{\alpha} \frac{1}{\rho_g} \left( \frac{k \rho_g}{2} \right)^{1/3} \cdot \frac{1}{\cos^2(\gamma - \alpha')} d\alpha' \quad , \text{ or} \tag{85}$$

$$\xi = \int_0^v \frac{1}{\rho_g} \left( \frac{k \rho_g}{2} \right)^{1/3} \cdot \frac{\sqrt{a^2 \sin^2 v' + c^2 \cos^2 v'}}{\sin(\gamma - \alpha')} dv' \quad (86)$$

To evaluate the ray divergence factor  $\left| \frac{d\psi_0(Q')}{d\psi(Q)} \right|$ , an adjacent surface ray is to be determined as done in the previous section. Differentiating Equation (84) with  $\ell = \text{constant}$ , one obtains

$$\ell \sin \gamma d\gamma = \sin \alpha \sqrt{a^2 \sin^2 v + c^2 \cos^2 v} dv - (r - S_e) \cos \alpha d\alpha,$$

$$\ell \cos \gamma d\gamma = \cos \alpha \sqrt{a^2 \sin^2 v + c^2 \cos^2 v} dv + (r - S_e) \sin \alpha d\alpha, \text{ or}$$

$$\begin{bmatrix} \sin \alpha \sqrt{a^2 \sin^2 v + c^2 \cos^2 v} & - (r - S_e) \cos \alpha \\ \cos \alpha \sqrt{a^2 \sin^2 v + c^2 \cos^2 v} & (r - S_e) \sin \alpha \end{bmatrix} \begin{bmatrix} dv \\ d\alpha \end{bmatrix} = \begin{bmatrix} \ell \sin \gamma \\ \ell \cos \gamma \end{bmatrix} d\gamma.$$

For a given  $d\gamma = d\psi_0$ , which is usually set equal to  $1^\circ$ , one can find the diffraction point  $^0(v+dv, \phi+d\phi)$  of the adjacent ray using the above equation. The radiation direction of the adjacent ray is then given by

$$\hat{t}^a = \hat{t}_r^a \cos(\beta + d\beta) + \hat{t}_e^a \sin(\beta + d\beta)$$

where  $\beta = \gamma - \alpha$  and  $d\beta = d\gamma - d\alpha$ . With the original radiation direction given by

$$\hat{t} = \hat{t}_r \cos \beta + \hat{t}_e \sin \beta, \text{ then}$$

$$\left| \frac{d\psi_0(Q')}{d\psi(Q)} \right| = \sqrt{\frac{d\gamma}{\cos^{-1}(\hat{t} \cdot \hat{t}^a)}}.$$

This completes the cone perturbation model used to compute the geodesic ray paths on the prolate spheroid provided the source is not mounted on the mid-section of the prolate spheroid.

## CHAPTER IV

### RESULTS

The solutions presented in the previous chapters are employed here to compute the far field radiation patterns for slots or monopoles mounted on a prolate spheroid. Various conical patterns are calculated and compared with the measurements.

To show the validity of the cylinder perturbation solution, the source is placed at  $\theta_s = 90^\circ$  as shown in Figure 14. To examine different conical pattern cuts, a cartesian coordinate system  $x'-y'-z'$  originally defining the spheroid geometry in Figure 14 is now rotated into  $x-y-z$  as shown in Figure 15. Note that the new cartesian coordinates are found by first rotating about the  $z'$  axis the angle  $\phi_c$  and then about the  $y$ -axis the angle  $\theta_c$ . The pattern is, then, taken in the  $x-y-z$  coordinate system with  $\theta_c$  fixed and  $\phi$  varied.

Calculated and measured azimuth-plane ( $\theta_c = 90^\circ$ ,  $\phi_c = 0^\circ$ ,  $\theta = 90^\circ$ ) patterns for a short monopole and a circumferential slot antenna located at  $\theta_s = 90^\circ$ ,  $\phi_s = 0^\circ$  on a  $2\lambda \times 4\lambda$  spheroid are shown in Figure 16(a) and (b). Here  $(\theta_s, \phi_s)$  denotes the source location in the original  $x'-y'-z'$  coordinate system. More results with  $\theta_c = 90^\circ$ ,  $\phi_c = 0^\circ$ , but different values of  $\theta$  are shown in Figures 16(c) and (d). It is noted that, when  $\theta > 90^\circ$ , the patterns are actually taken entirely in the shadow region.

The geodesic paths and tangents associated with this source position are shown in Figure 17(a)(b) and compared with the more elaborate work done by Burnside [2]. Note that the predicted geodesic paths coincide with each other in the near region close to the source. Actually, the Fock functions associated with the solutions drop more than 20 db, as the Fock parameter ( $\xi$ ) reaches 2.5 in the deep shadow region [6]. This clearly shows the significant portion of the surface as discussed in Chapter I.

Several measurements were taken for a short monopole placed at  $\theta_s = 30^\circ$ ,  $\phi_s = 0^\circ$  to compare with the cone perturbation solution. Calculated and measured azimuth-plane ( $\theta_c = 90^\circ$ ,  $\phi_c = 0^\circ$ ,  $\theta = 90^\circ$ ) patterns are shown in Figure 18. The results are seen to agree very well with each other. The calculated geodesic paths and tangents for this case are shown in Figure 19(a)(b).

Next, a roll plane pattern ( $\theta_c = 0^\circ$ ,  $\phi_c = 0^\circ$ ,  $\theta = 90^\circ$ ) was examined. The calculated and measured results for  $E_\theta$  and  $E_\phi$  are shown in

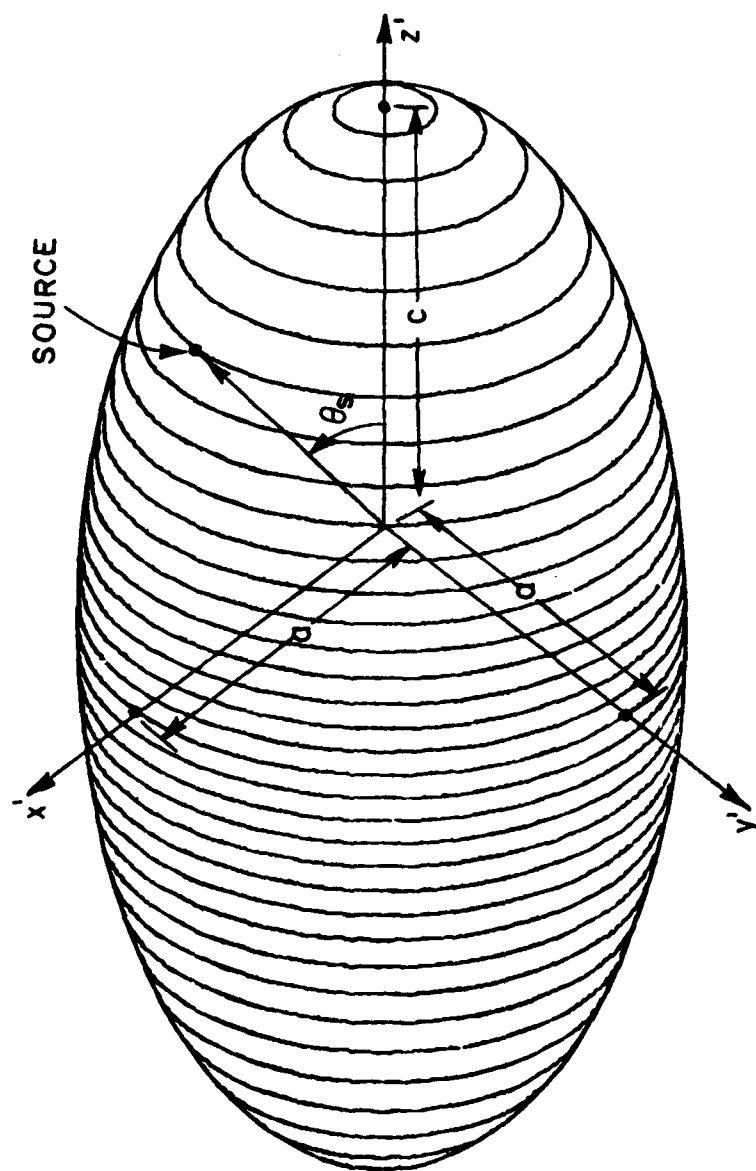


Figure 14. Geometry of a spheroid.

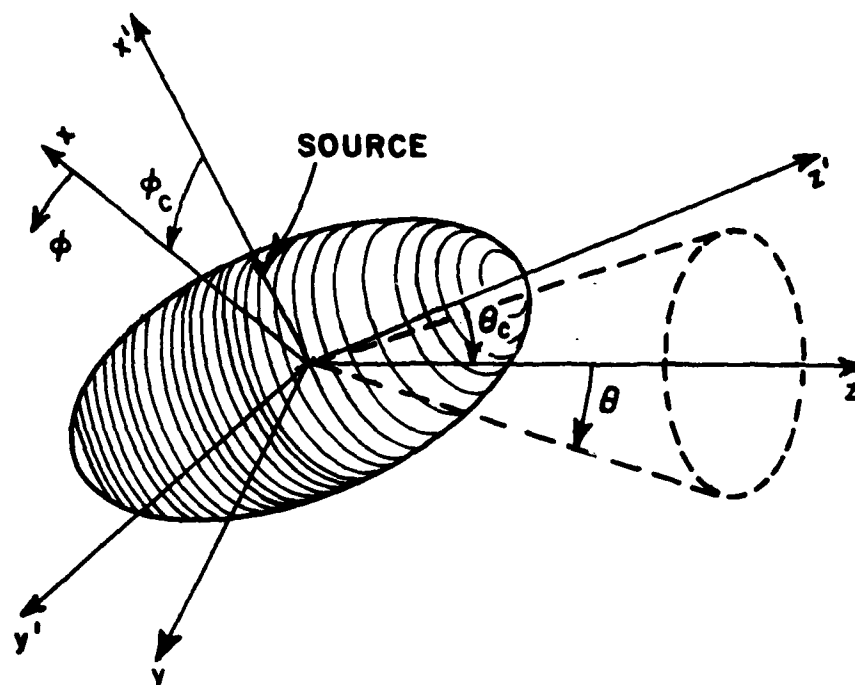


Figure 15. Definition of pattern axis.

Figure 20, where only one ray is employed in the calculation. However, the one-dominant-ray assumption is not adequate in this case, as there actually exists four significant GTD terms on a spheroid [2] as shown in Figure 21. The single exponentially decaying field contributed from either ray 1 or ray 2 is shown in Figure 22. If one includes ray 1 and 2 in the solution, one obtains the characteristic interference pattern shown in Figure 23. One would expect that the further inclusion of the third and even the fourth ray shown in Figure 21 might make the results agree better. However, ray 3 and 4 fall into the so-called caustic region where virtually an infinite set of rays have significant effects on the pattern, and the basic GTD theory fails. In Figure 19(b), one can see that rays just simply collapse in these caustic regions.

The  $E_\theta$  pattern in the elevation plane ( $\theta_c = 90^\circ$ ,  $\phi_c = 90^\circ$ ,  $\theta = 90^\circ$ ) is essentially negligible; whereas, the dominant  $E_\phi$  is shown in Figure 24. Here the caustic effect, which is associated with  $\sqrt{\frac{d\psi_0}{d\psi}} \rightarrow \infty$ , is suppressed artificially so that one does not observe the sharp spikes normally attributed to a caustics. The discontinuities in the pattern result from the fact that various ray trajectories are included in different sectors of the pattern. As shown in Figure 25, to remove the ray tracing problems close to the caustic regions, a cone is used as a boundary that defines whether two rays (ray 1 and 2) are to be included in the solution. It is understood that the results do not match in some regions, however, in that the caustic effect still remains unresolved.

To avoid the caustic effect, the pattern is taken again with the spheroid rotated by  $45^\circ$  (i.e.,  $\theta_c = 90^\circ$ ,  $\phi_c = 45^\circ$ ,  $\theta = 90^\circ$ ). The results shown in Figure 26 are again seen to agree very well even with only one dominant ray considered.

One has to be reminded that the results shown above are all done for a very stringent case, i.e. the spheroid is small electrically and the spheroid is approaching a sphere. To model an aircraft or missile fuselage in a physical sense, the electric dimensions of a spheroid would be much larger than the ones chosen, i.e.,  $2\lambda \times 4\lambda$ . It is noticed that the source location  $\theta_s = 30^\circ$  was also chosen too close to the end of the spheroid. If more realistic aircraft or missile fuselage dimensions were employed, one would expect that the results would be improved a great deal. On the other hand, it is useful to make such comparisons between measured and calculated results. Although discrepancies do occur in some cases, they only happen when the caustic effects come into play. However, the caustic effects associated with this type of caustic still remains an unsolved problem.

More calculated examples are shown in Figure 27-35. The algorithm boundaries shown in Figure 25 are used in determining whether one or two rays are used in the solution. Note that  $\beta_{12}$  is defined automatically by the numerical solution. This is done by determining the

caustic angle in the elevation pattern ( $\beta_c$ ) and adding a few additional degrees to that value, i.e.  $\beta_{12} = \beta_c + \Delta\beta$  where  $2^\circ \leq \Delta\beta \leq 10^\circ$ . One would expect to observe slight discontinuities somewhere, because various numbers of rays are included in different regions. Note that these results represent much more realistic fuselage shapes and dimensions.

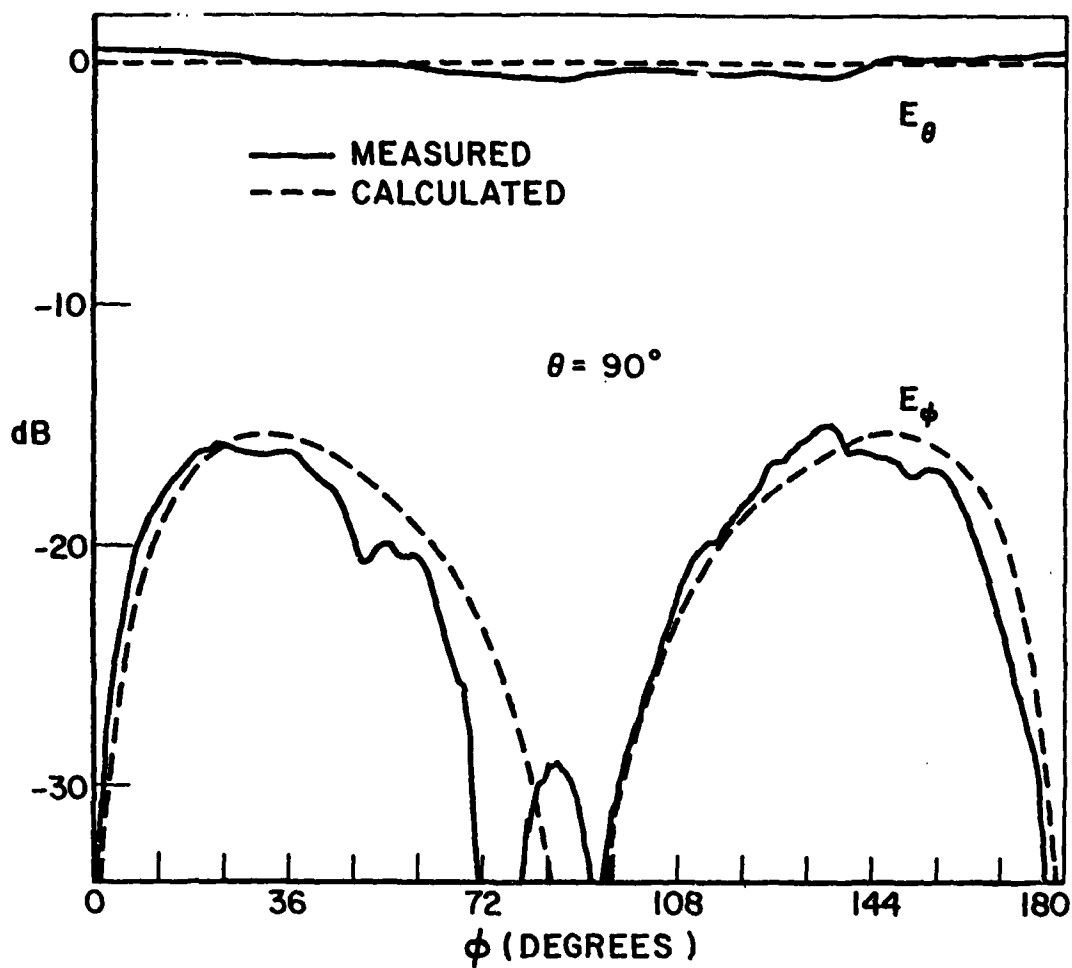


Figure 16(a). Azimuth plane patterns ( $\theta_c = 90^\circ$ ,  $\phi_c = 0^\circ$ ,  $\theta = 90^\circ$ ) for a short monopole mounted at  $\theta_s = 90^\circ$  on a  $2\lambda \times 4\lambda$  spheroid.



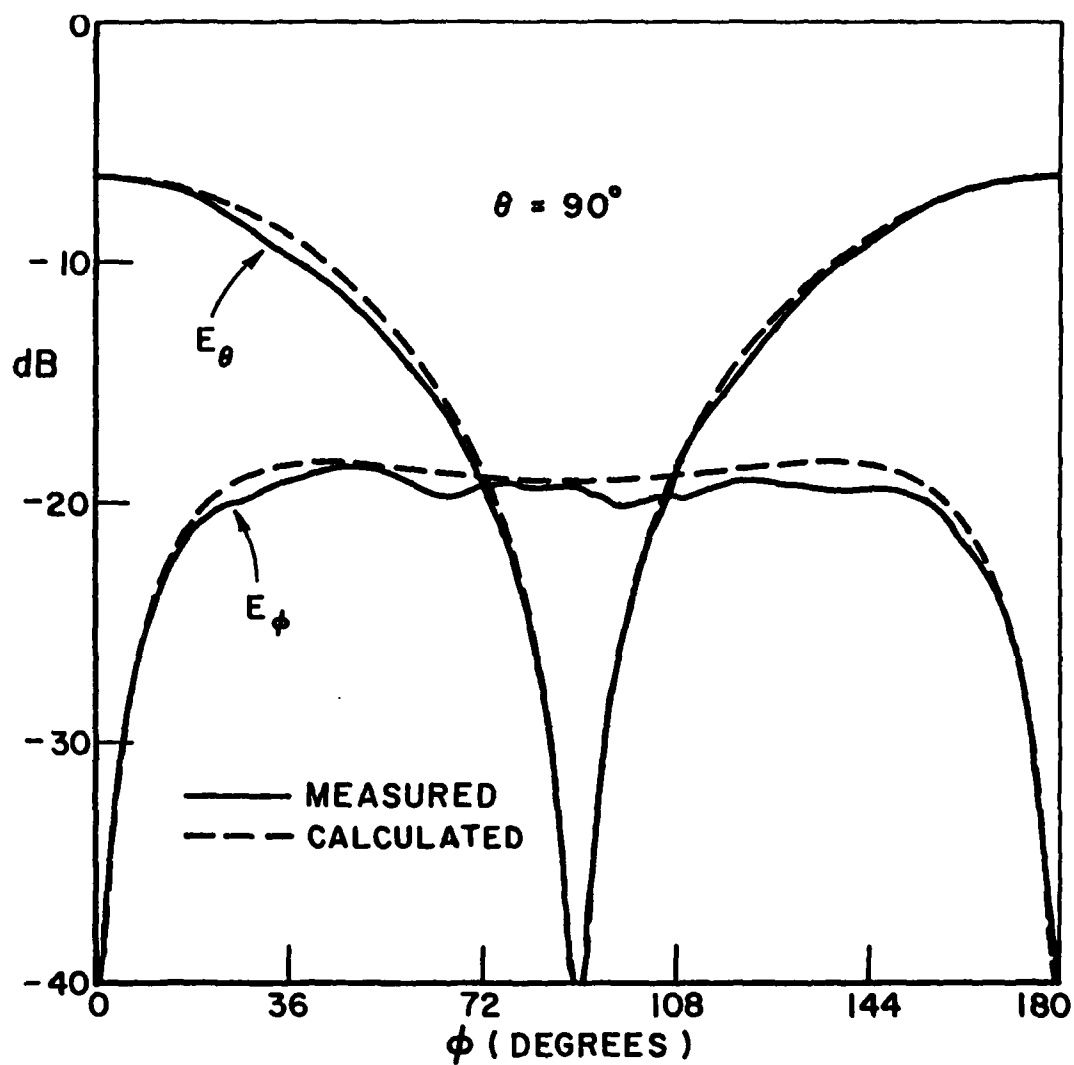


Figure 16(b). Azimuth plane patterns ( $\theta_c = 90^\circ$ ,  $\phi_c = 90^\circ$ ,  $\theta = 90^\circ$ ) for a circumferential slot ( $A = 0.291\lambda$ ,  $B = 0.624\lambda$ ) mounted at  $\theta_s = 90^\circ$  on a  $2\lambda \times 4\lambda$  spheroid.

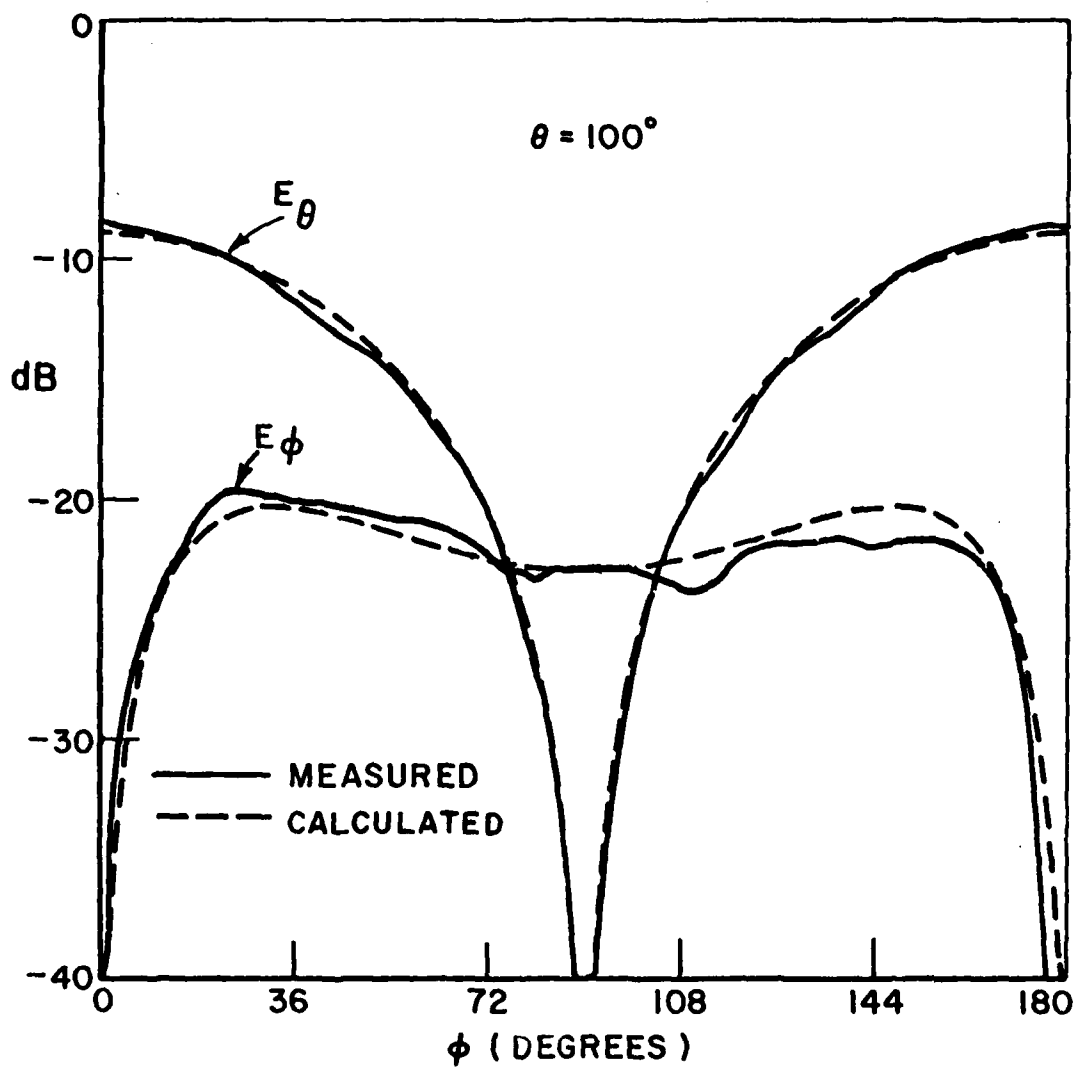


Figure 16(c). Conical patterns ( $\theta_c = 90^\circ$ ,  $\phi_c = 0^\circ$ ,  $\theta = 100^\circ$ ) for a circumferential slot ( $A = 0.291\lambda$ ,  $B = 0.624\lambda$ ) mounted at  $\theta_s = 90^\circ$  on a  $2\lambda \times 4\lambda$  spheroid.

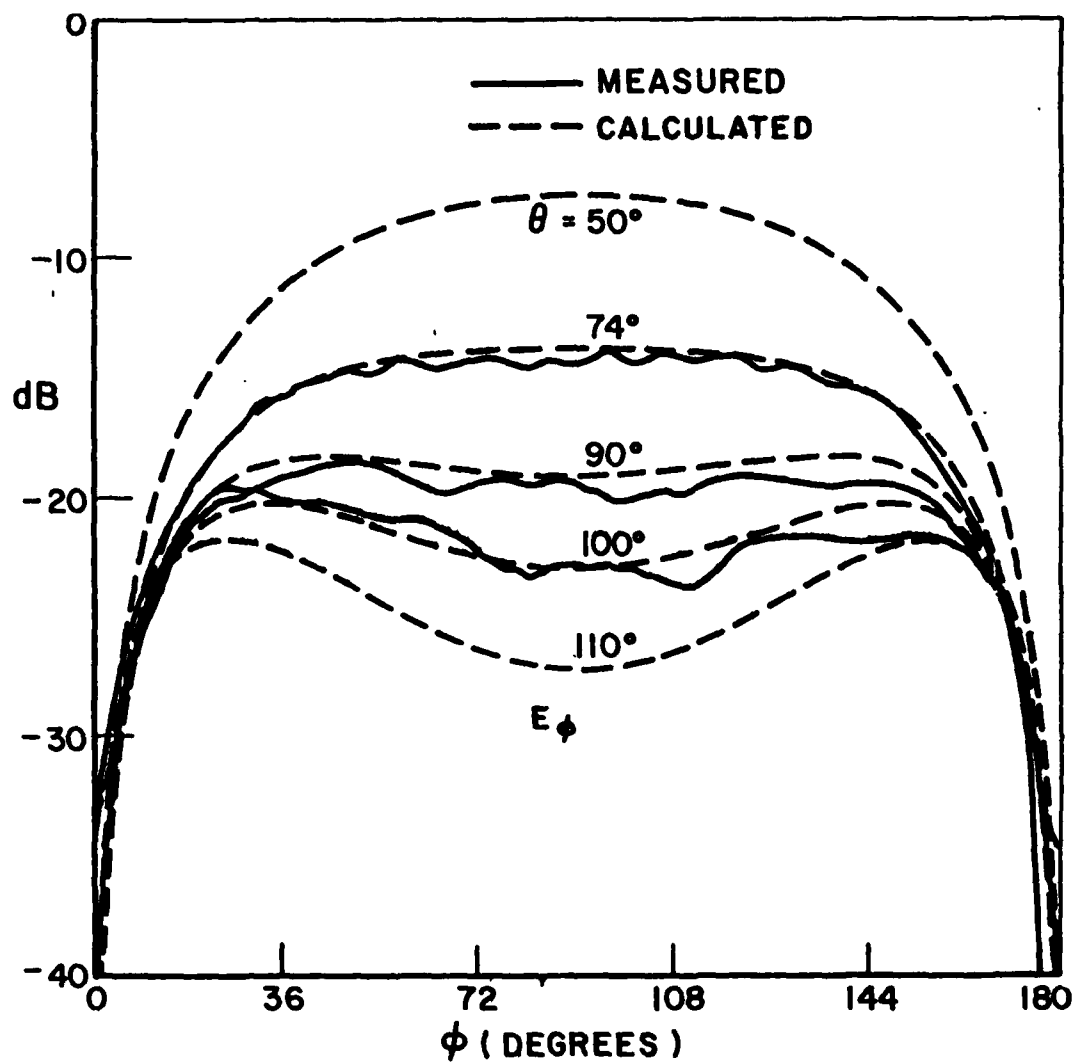


Figure 16(d). Conical patterns ( $E_\phi$ ) for  $\theta_c = 90^\circ$ ,  $\phi_c = 0^\circ$  for a circumferential slot ( $A = 0.291\lambda$ ,  $B = 0.624\lambda$ ) mounted at  $\theta_s = 90^\circ$  on a  $2\lambda \times 4\lambda$  spheroid.

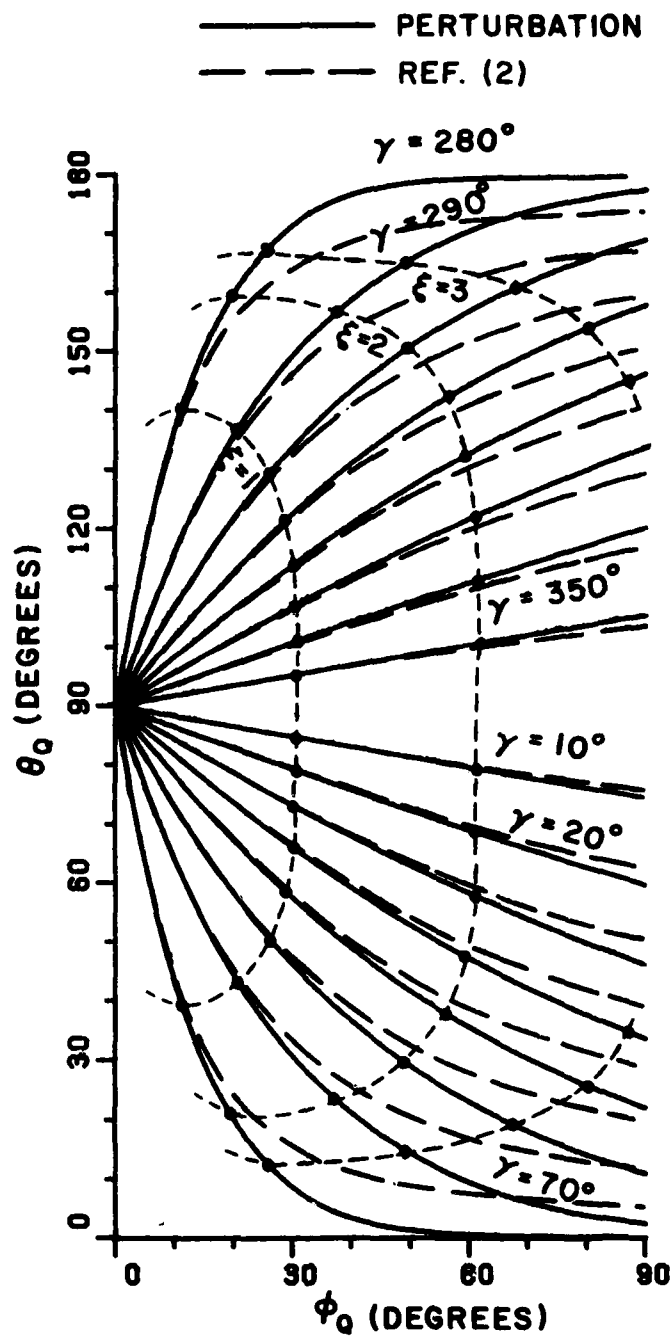


Figure 17(a). Geodesic path defined by the surface parameters  $(\theta_Q, \phi_Q)$ , for a source mounted at  $\theta_S = 90^\circ$  on a  $2\lambda \times 4\lambda$  spheroid. Note that  $\gamma$  is the angle between the geodesic tangent  $\hat{t}$  and one principal direction  $\hat{t}_r$  at the source location.

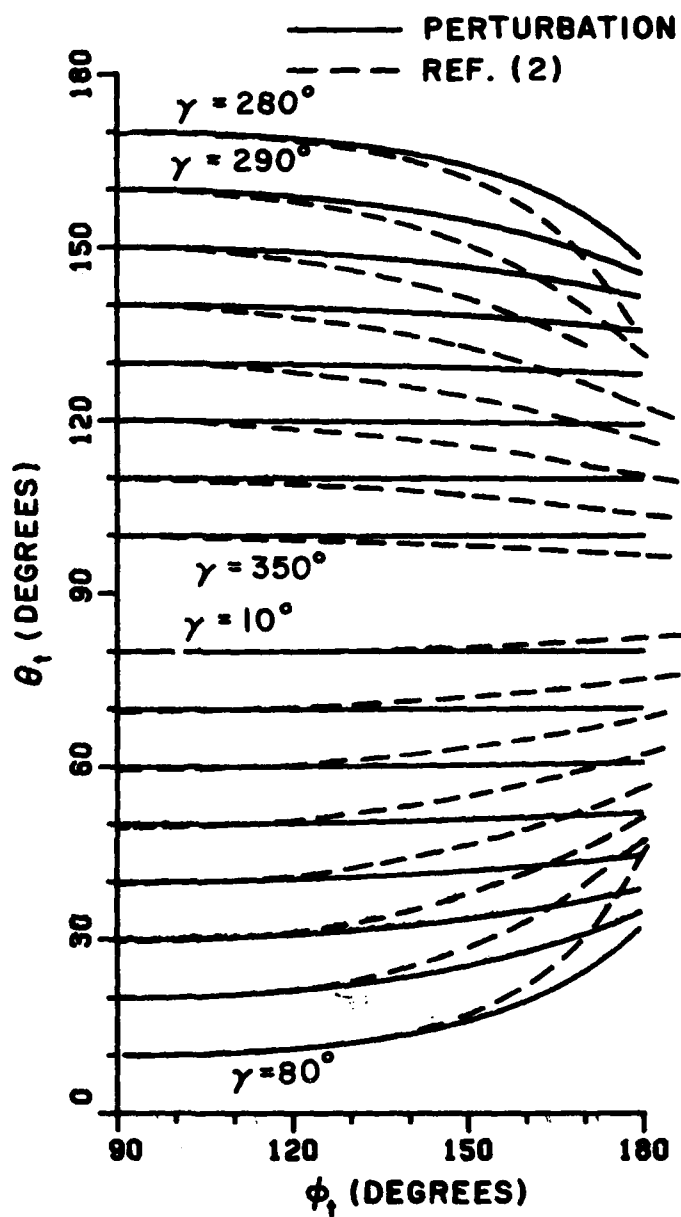


Figure 17(b). Geodesic tangent defined by the radial vector direction  $(\theta_t, \phi_t)$  for a source mounted at  $\theta_s = 90^\circ$  on a  $2\lambda \times 4\lambda$  spheroid. Note that  $\gamma$  is the angle between the geodesic tangent  $\hat{t}$  and one principal direction  $\hat{t}_r$  at the source location.

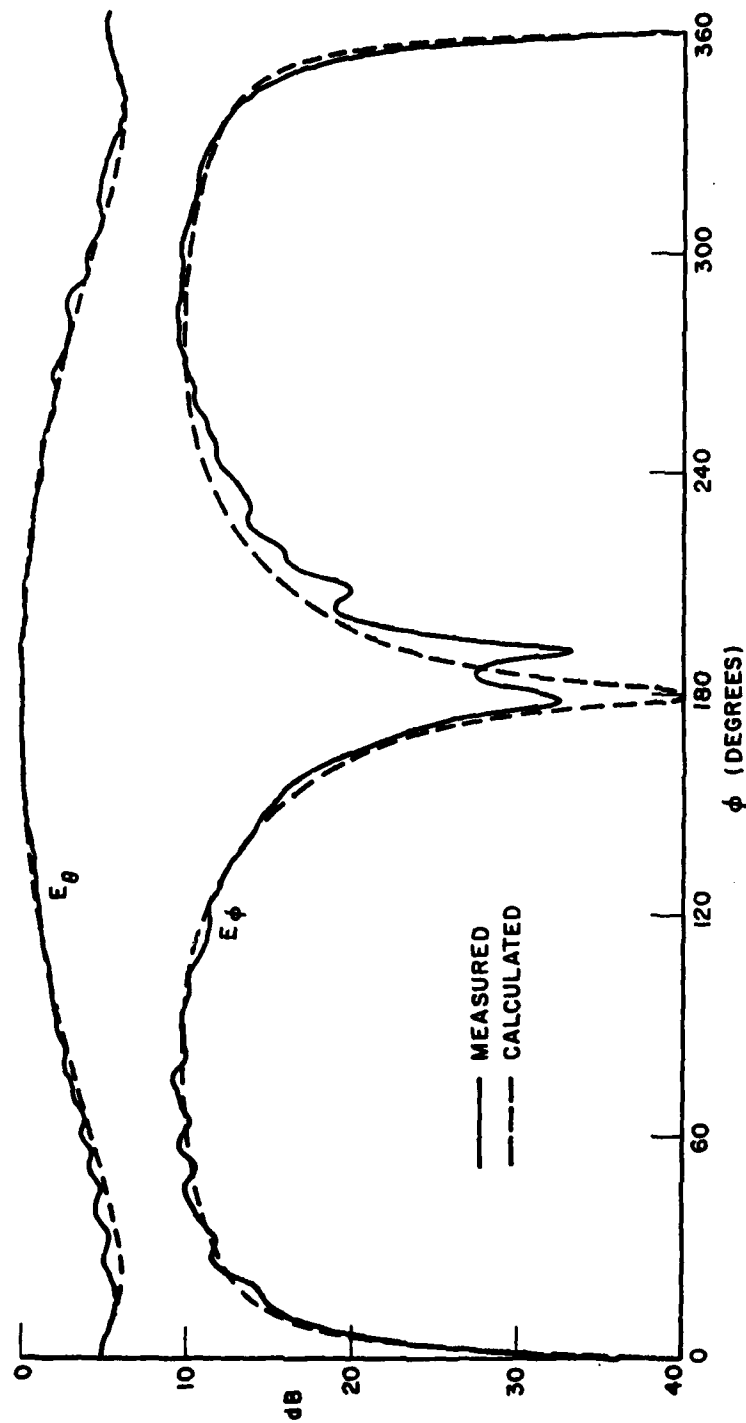


Figure 18. Calculated and measured azimuth plane patterns ( $\theta = 90^\circ$ ,  $\phi_c = 0^\circ$ ,  $\theta = 90^\circ$ ) for a short monopole mounted at  $\theta_s = 300$  on a  $2\lambda \times 4\lambda$  spheroid.

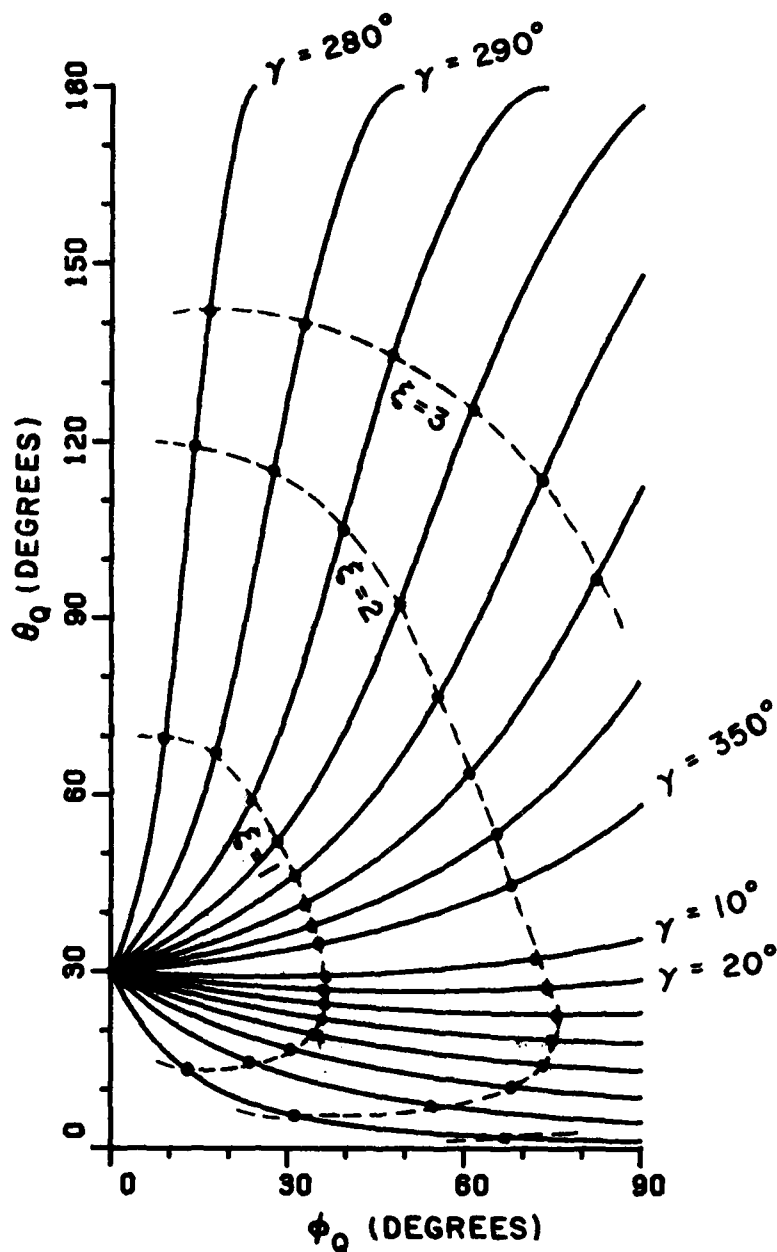


Figure 19(a). Geodesic path defined by the surface parameters  $(\theta_Q, \phi_Q)$  for a source mounted at  $\theta_s = 30^\circ$  on a  $2\lambda \times 4\lambda$  spheroid. Note that  $\gamma$  is the angle between the geodesic tangent  $t$  and one principal direction  $t_r$  at the source location.

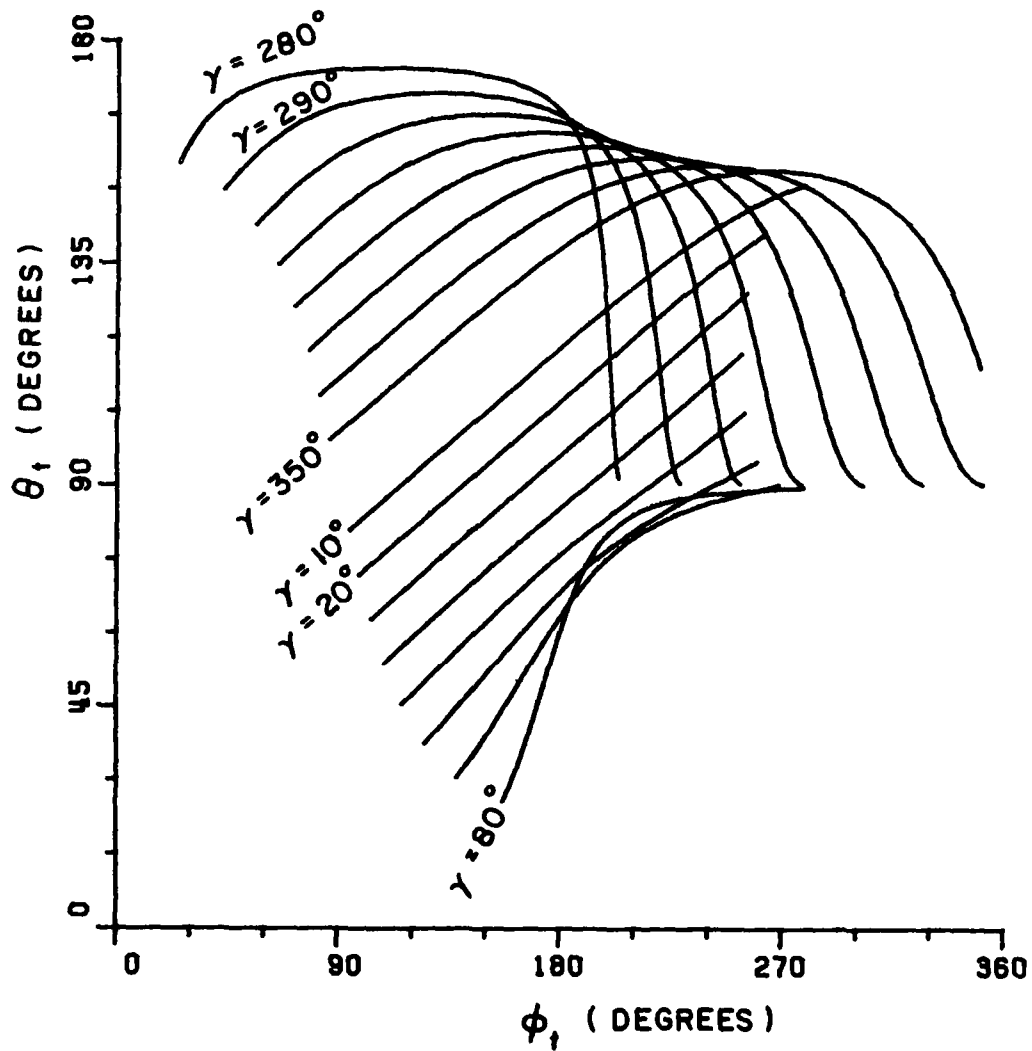


Figure 19(b). Geodesic tangent defined by the radial vector direction  $(\theta_t, \phi_t)$  for a source mounted at  $\theta_s = 30^\circ$  on a  $2\lambda \times 4\lambda$  spheroid. Note that  $\gamma$  is the angle between the geodesic tangent  $\hat{t}$  and one principal direction  $\hat{t}_r$  at the source location.



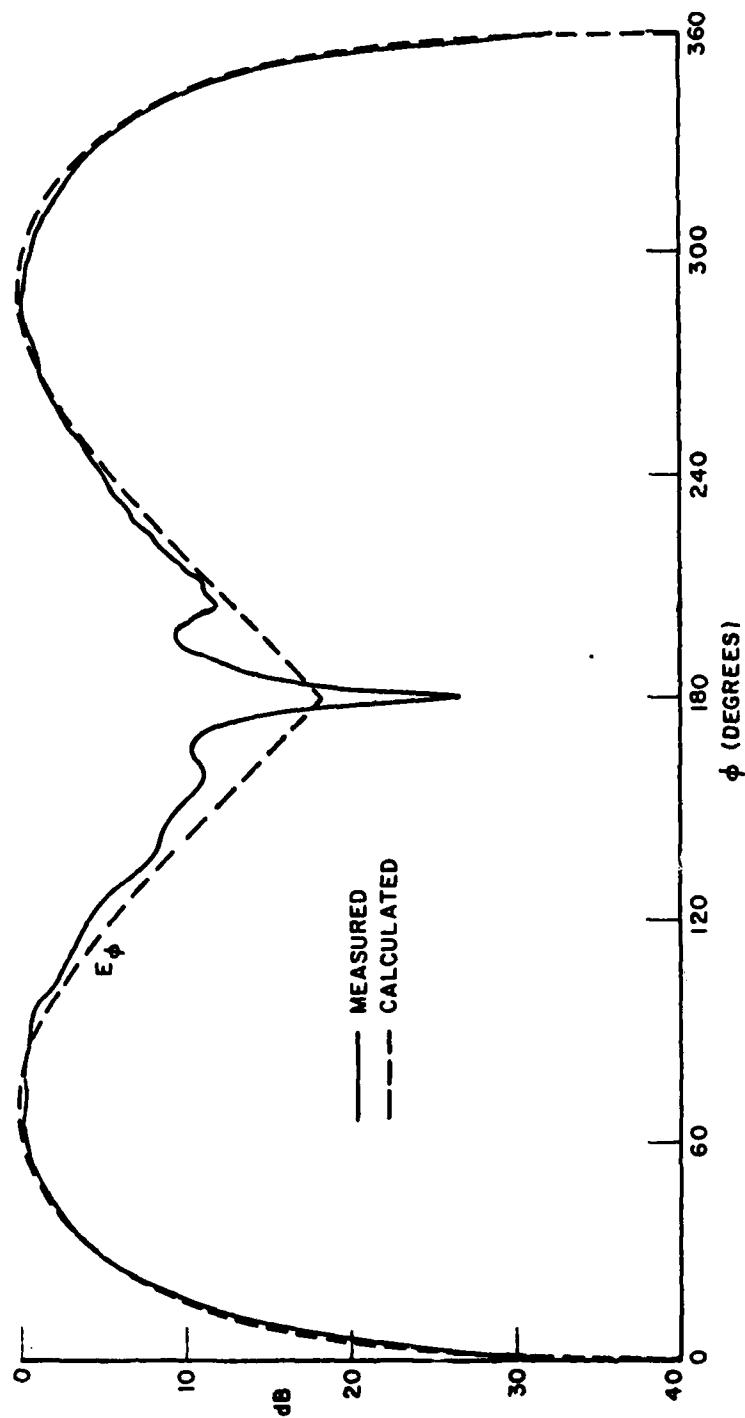


Figure 20(a). Roll plane ( $\theta_c=0^\circ$ ,  $\phi_c=0^\circ$ ,  $\theta=90^\circ$ ) patterns ( $E_\phi$ ) for a short monopole mounted at  $\theta_s=30^\circ$  on a  $2\lambda \times 4\lambda$  spheroid. Note that only one dominant ray is employed in the calculation.

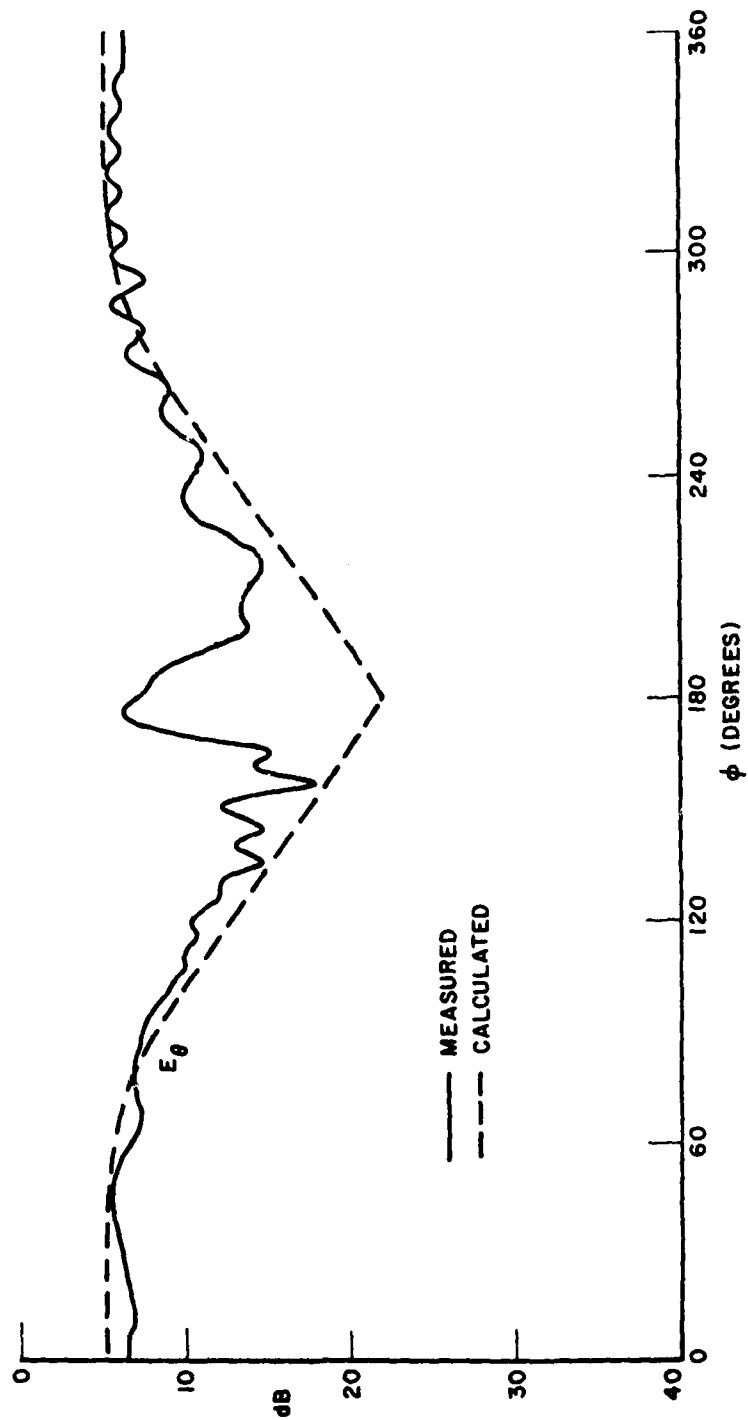


Figure 20(b). Roll plane ( $\theta_c = 0^\circ$ ,  $\phi_c = 0^\circ$ ,  $\theta = 90^\circ$ ) patterns ( $E_\theta$ ) for a short monopole mounted at  $\theta_s = 30^\circ$  on a  $2\lambda \times 4\lambda$  spheroid. Note that only one dominant ray is employed in the calculation.

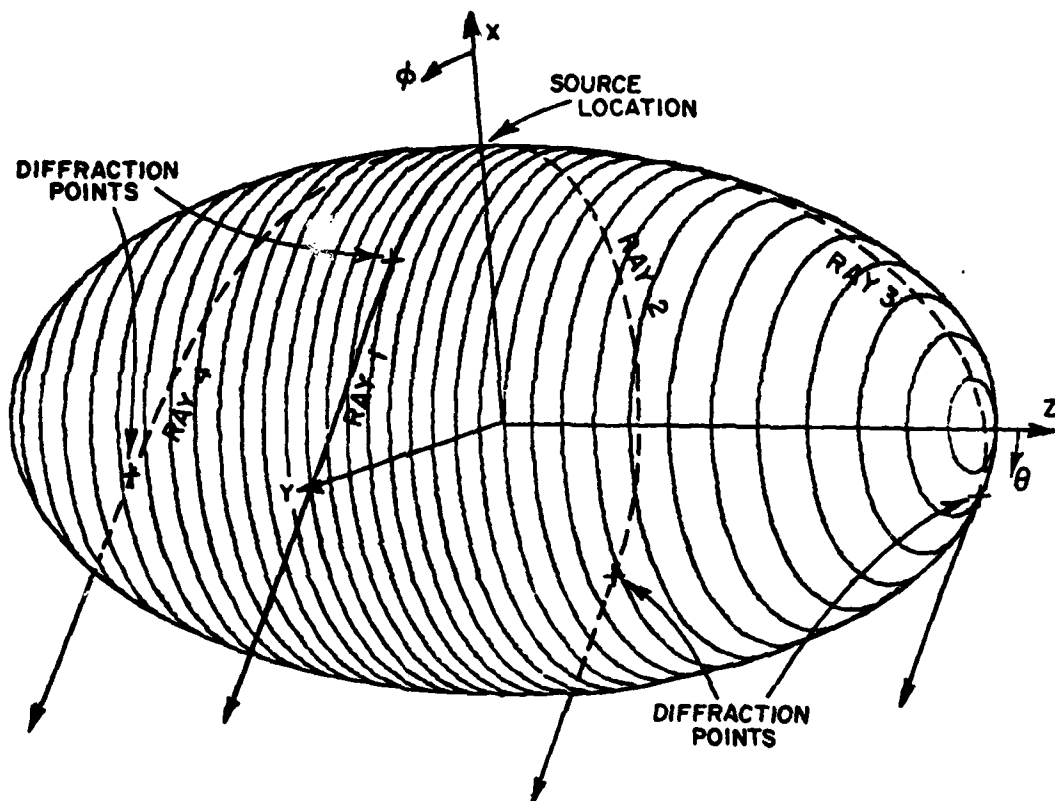


Figure 21. The four dominant GTD terms that radiate at ( $\theta=90^\circ$ ,  $\phi=145^\circ$ ).

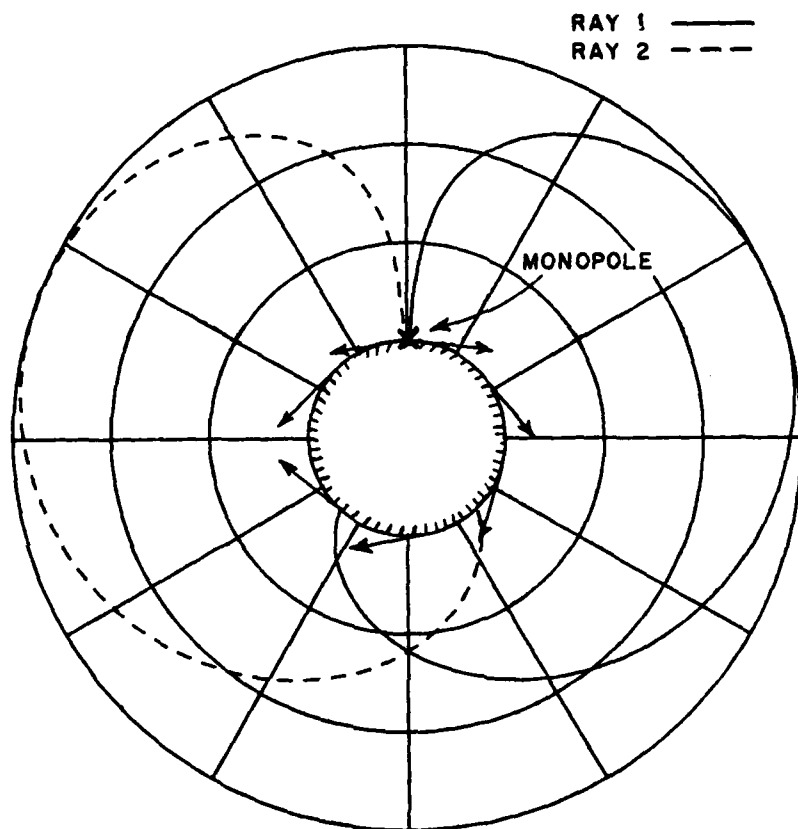


Figure 22. The single decaying ray for a major polarization.

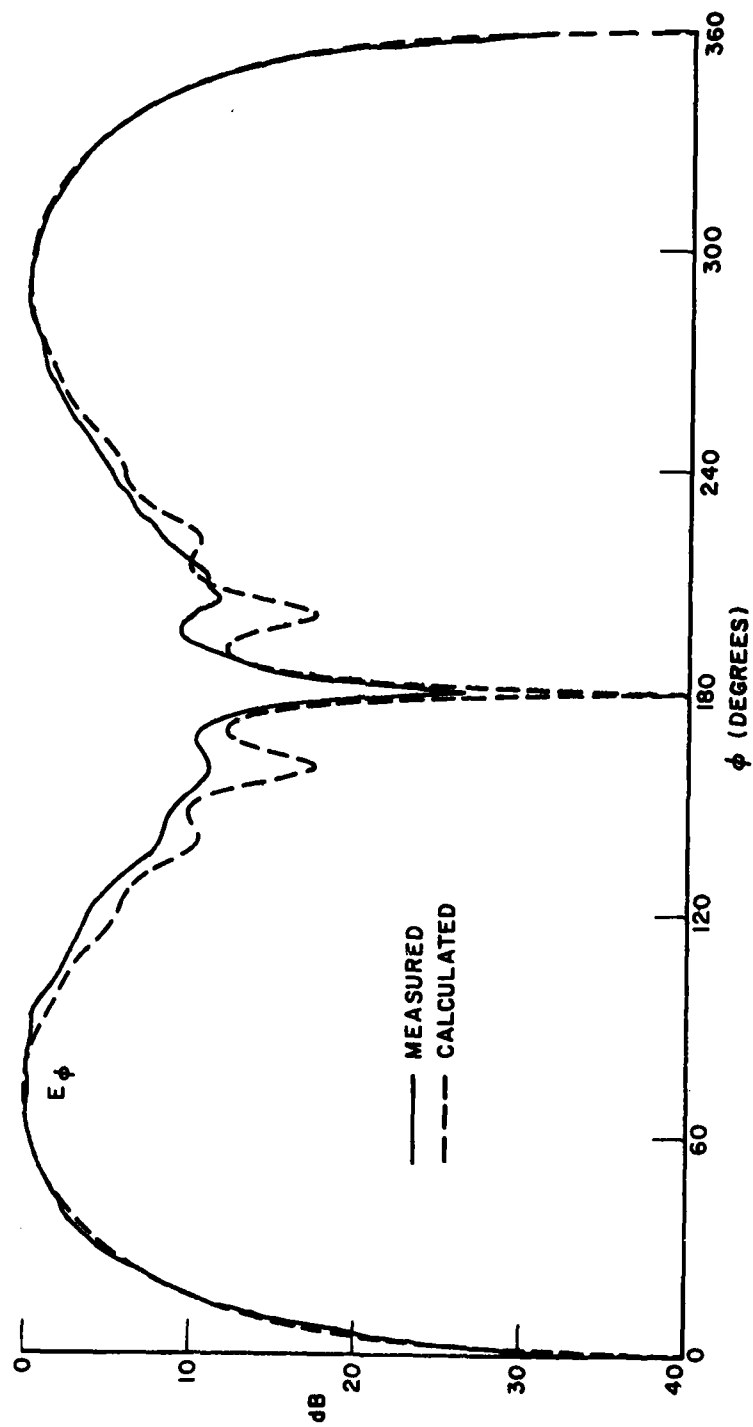


Figure 23(a). Roll plane ( $\theta_c = 0^\circ$ ,  $\phi_c = 0^\circ$ ,  $\theta = 90^\circ$ ) natterns ( $E_\phi$ ) for a short monopole mounted at  $\theta_s = 30^\circ$  on a  $2\lambda \times 4\lambda$  soheroid. Two rays (ray 1 and 2 in Figure 21) are employed in the calculation.

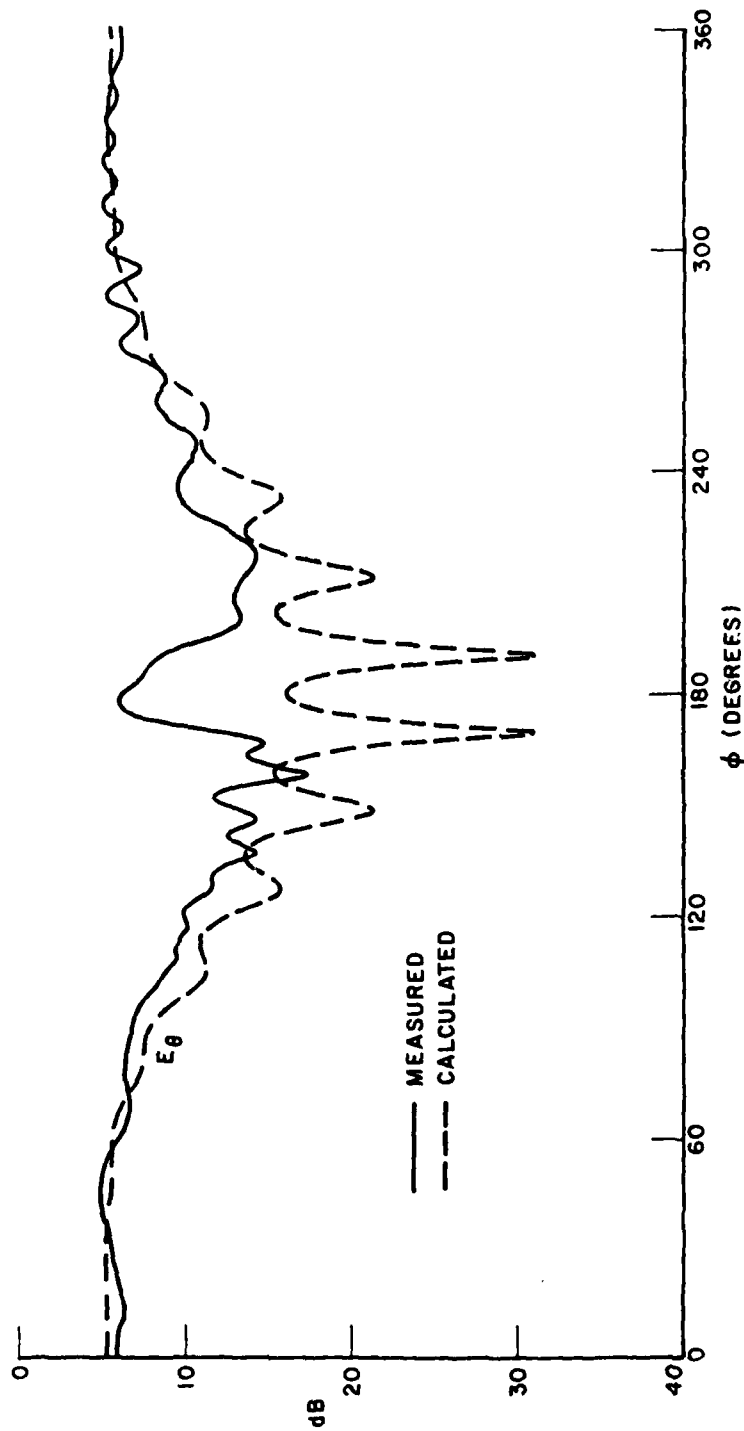


Figure 23(b). Roll plane ( $\theta_c=0^\circ$ ,  $\phi_c=0^\circ$ ,  $\theta=90^\circ$ ) patterns ( $E_\theta$ ) for a short monopole mounted at  $\theta_s=30^\circ$  on a  $2\lambda \times 4\lambda$  spheroid. Two rays (ray 1 and 2 in Figure 21) are employed in the calculation.

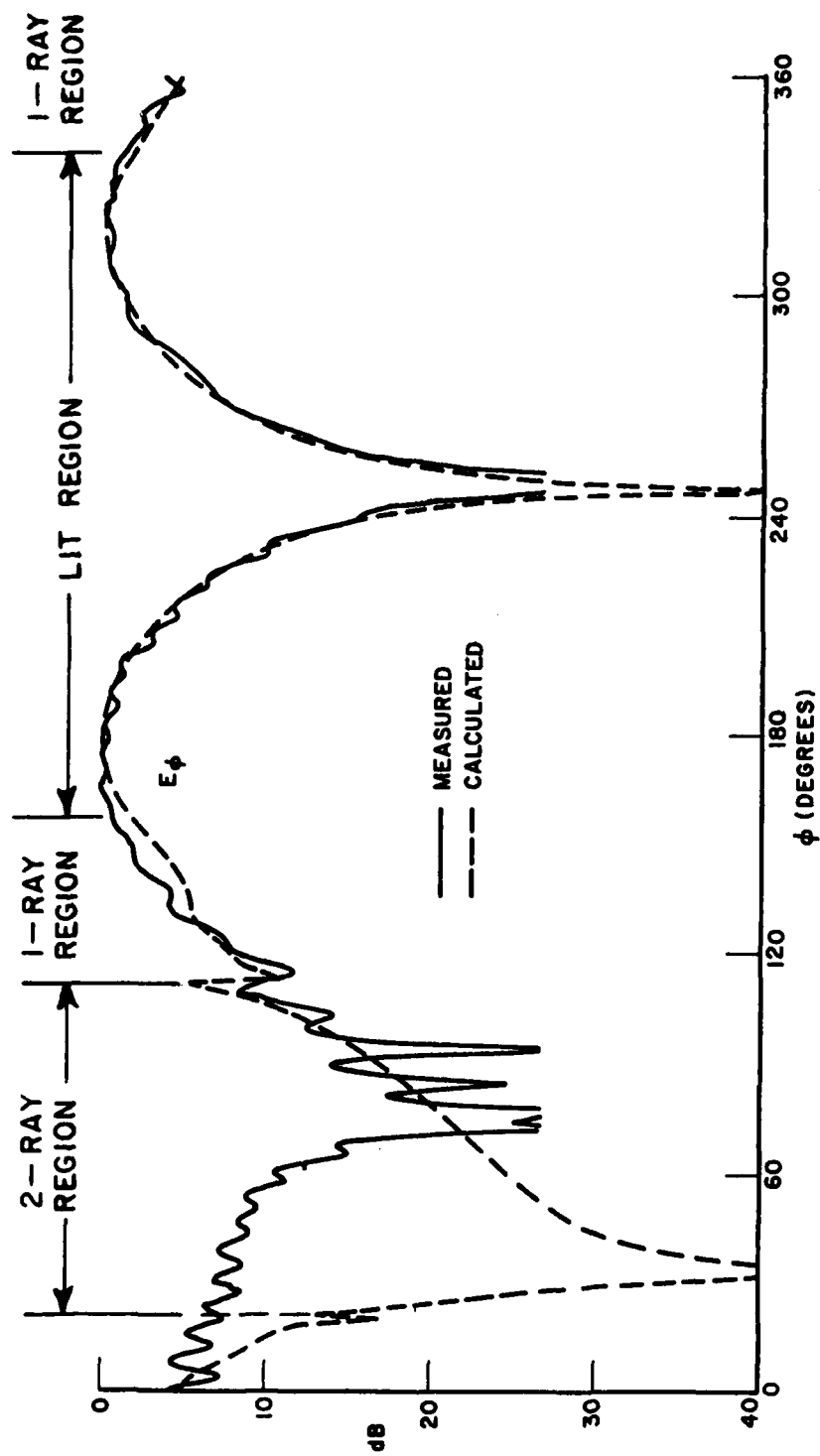


Figure 24. Calculated and measured elevation plane patterns ( $\theta_c = 90^\circ$ ,  $\phi_c = 90^\circ$ ,  $\theta = 90^\circ$ ) for a short monopole mounted at  $\theta_s = 30^\circ$  on a  $2\lambda \times 4\lambda$  spheroid.

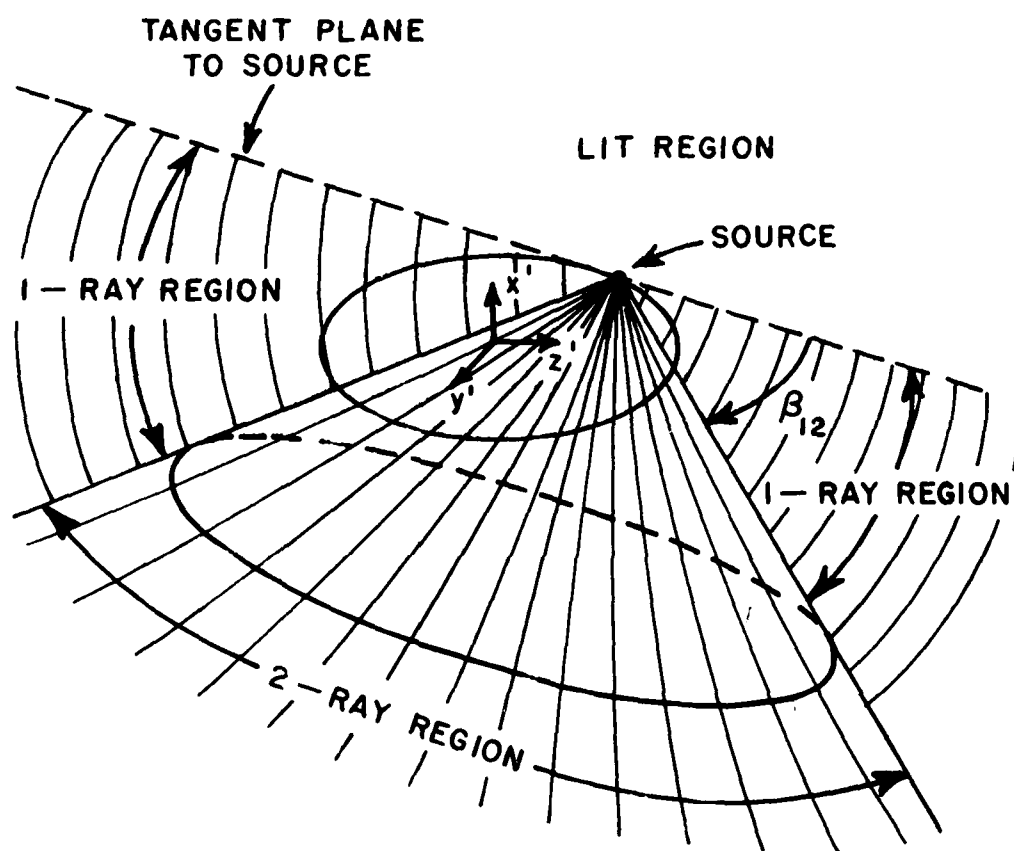


Figure 25. Cone boundary used to define terms to be included in the shadow region.



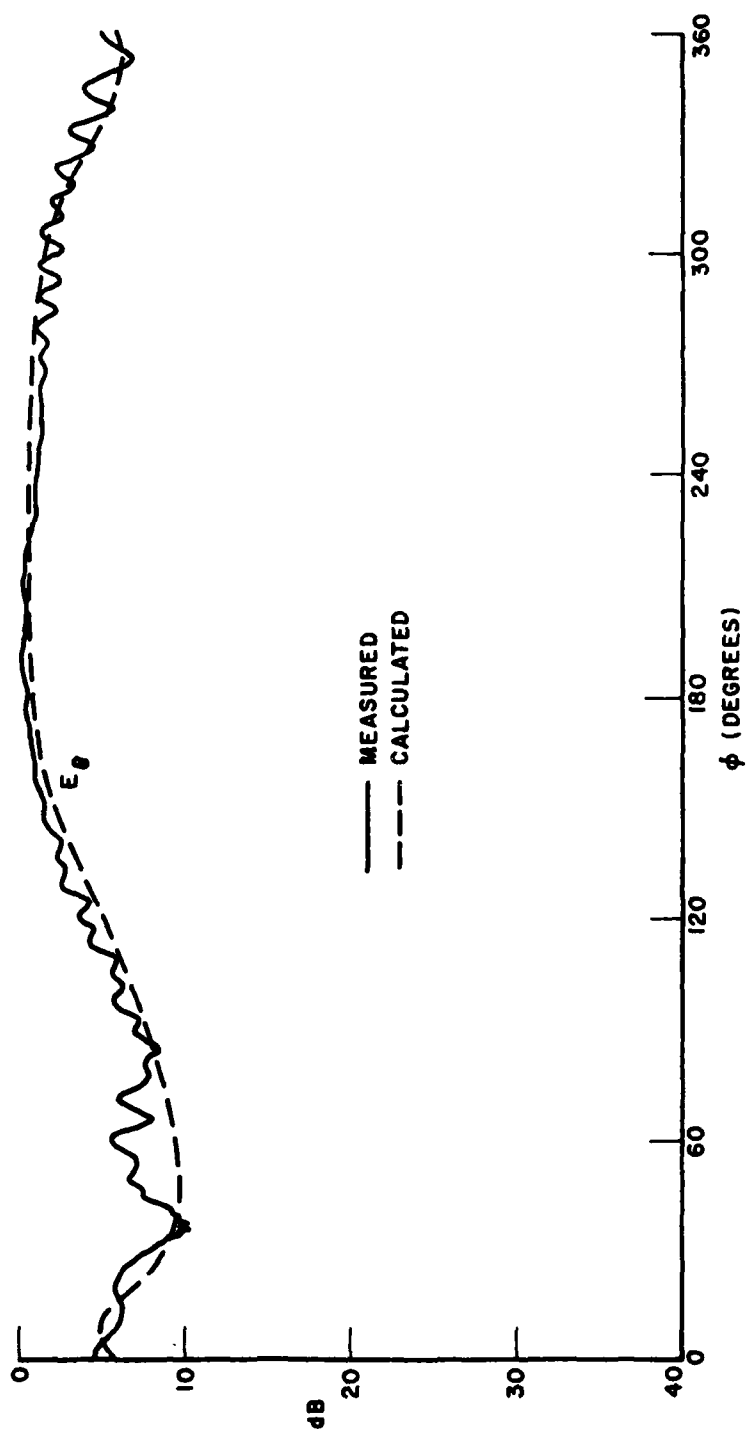


Figure 26(a). Conical patterns ( $E_\theta$ ) for  $\theta_c = 90^\circ$ ,  $\phi_c = 45^\circ$ , and  $\theta = 90^\circ$  for a short monopole mounted at  $\theta_s = 30^\circ$  on a  $2\lambda \times 4\lambda$  spheroid. Only one dominant ray is employed in the calculation.

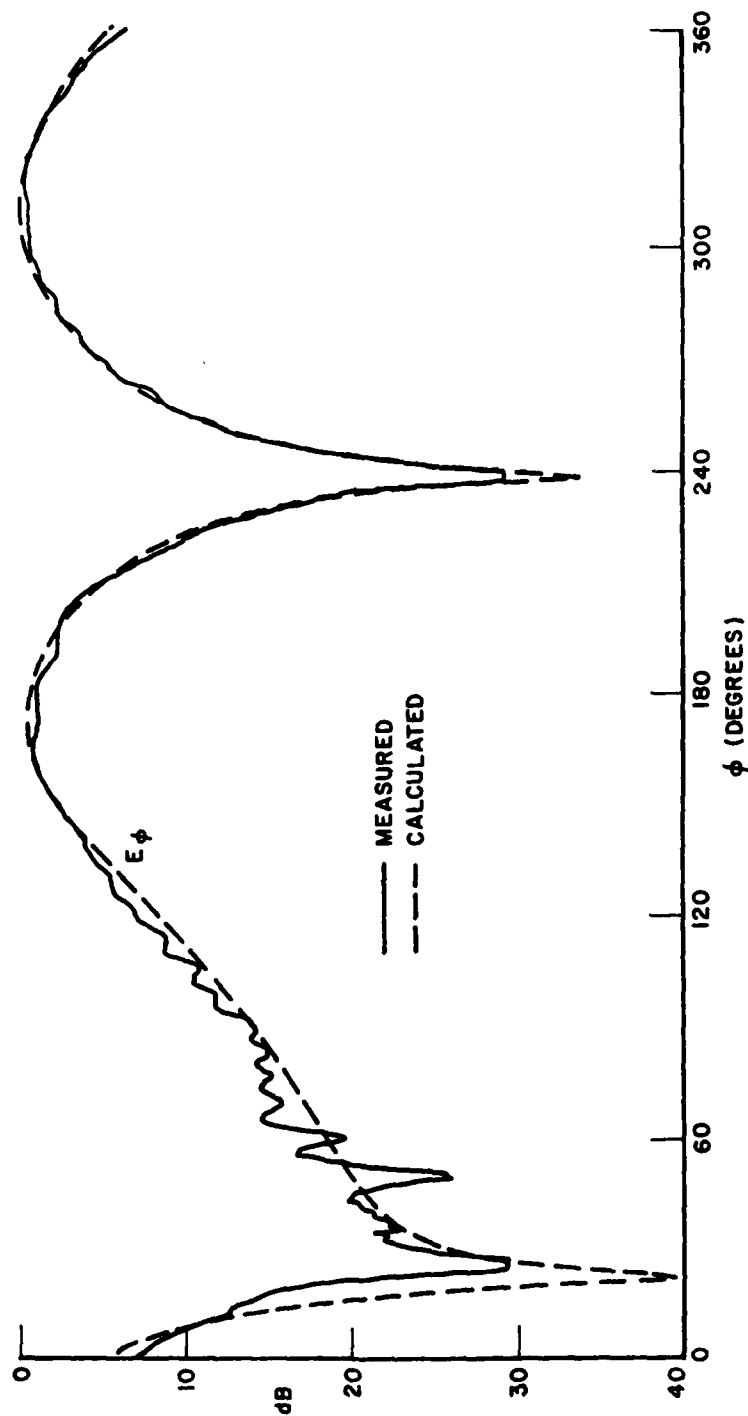
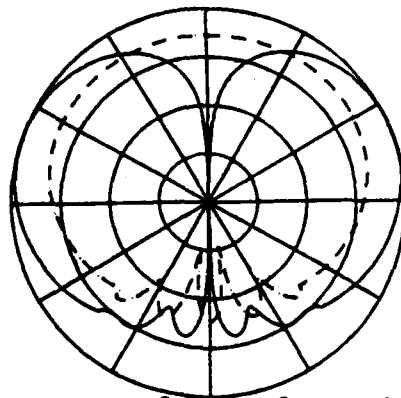
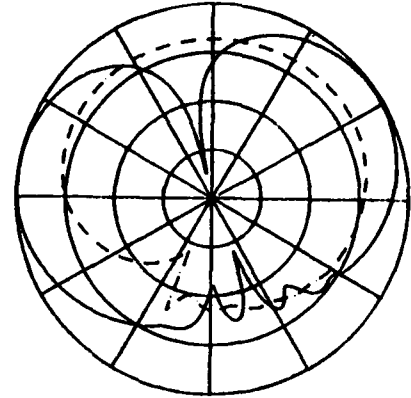


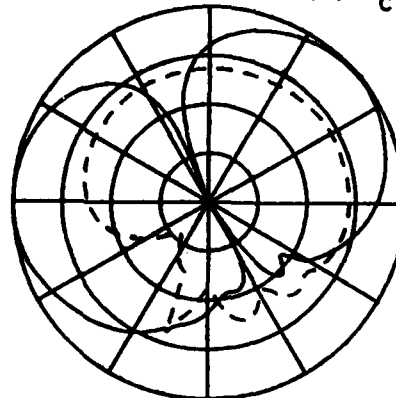
Figure 26(b). Conical patterns ( $E_\phi$ ) for  $\theta_c = 90^\circ$ ,  $\phi_c = 45^\circ$ , and  $\theta = 90^\circ$  for a short monopole mounted at  $\theta_s = 30^\circ$  on a  $2\lambda \times 4\lambda$  spheroid. Only one dominant ray is employed in the calculation.



(a)  $\theta_c = 0^\circ$ ,  $\phi_c = 90^\circ$ ,  $\theta = 90^\circ$

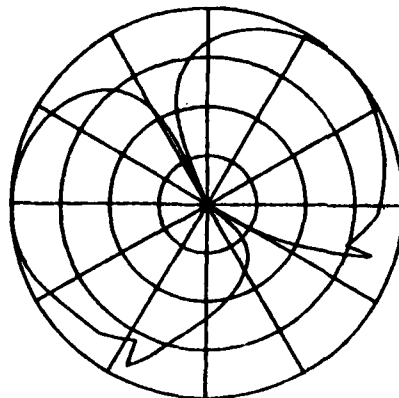


(b)  $\theta_c = 30^\circ$ ,  $\phi_c = 90^\circ$ ,  $\theta = 90^\circ$

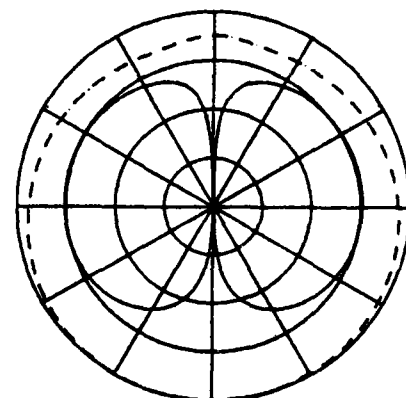


$\theta_c = 60^\circ$ ,  $\phi_c = 90^\circ$ ,  $\theta = 90^\circ$

—  $E_\phi$   
- -  $E_\theta$

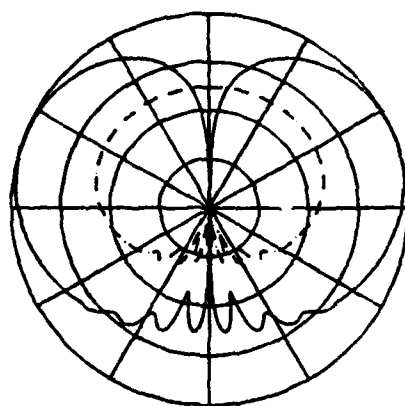


(d)  $\theta_c = 90^\circ$ ,  $\phi_c = 90^\circ$ ,  $\theta = 90^\circ$

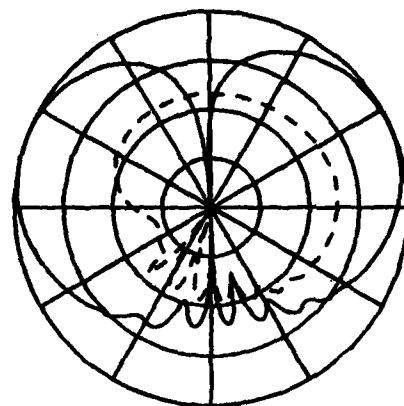


(e)  $\theta_c = 90^\circ$ ,  $\phi_c = 0^\circ$ ,  $\theta = 90^\circ$

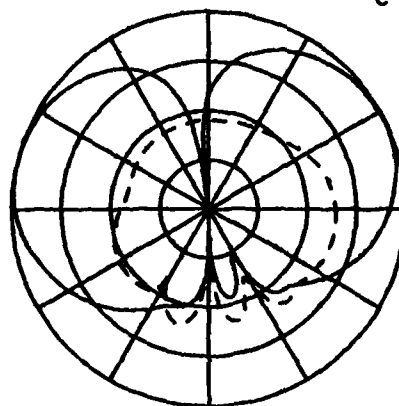
Figure 27. Radiation patterns for a short monopole mounted at  $\theta_s = 30^\circ$  on a  $2\lambda \times 4\lambda$  spheroid.



(a)  $\theta_c = 0^\circ$ ,  $\phi_c = 90^\circ$ ,  $\theta = 90^\circ$

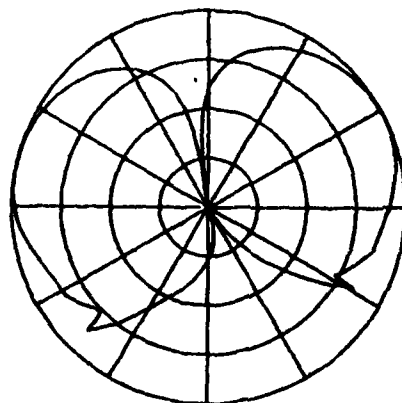


(b)  $\theta_c = 30^\circ$ ,  $\phi_c = 90^\circ$ ,  $\theta = 90^\circ$

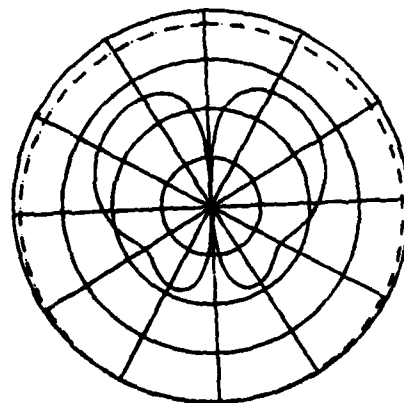


(c)  $\theta_c = 60^\circ$ ,  $\phi_c = 90^\circ$ ,  $\theta = 90^\circ$

—  $E_\phi$   
- - -  $E_\theta$

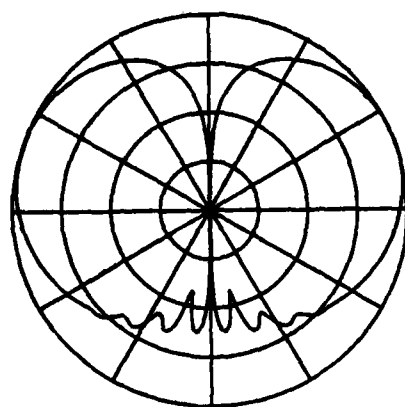


(d)  $\theta_c = 90^\circ$ ,  $\phi_c = 90^\circ$ ,  $\theta = 90^\circ$

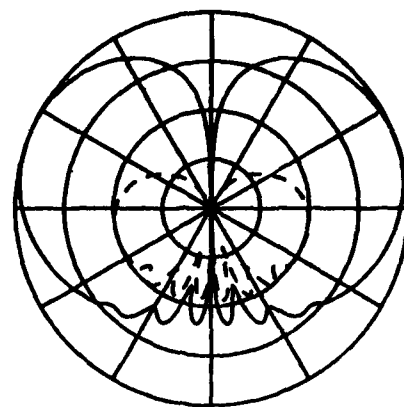


(e)  $\theta_c = 90^\circ$ ,  $\phi_c = 0^\circ$ ,  $\theta = 90^\circ$

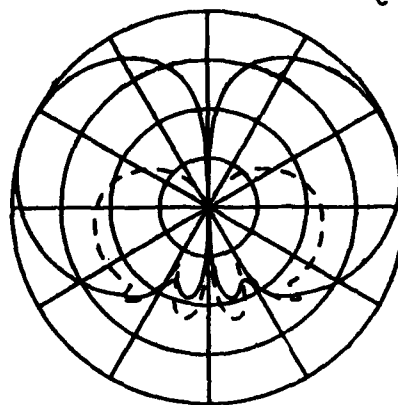
Figure 28. Radiation patterns for a short monopole mounted at  $\theta_s = 60^\circ$  on a  $2\lambda \times 4\lambda$  spheroid.



(a)  $\theta_c = 0^\circ$ ,  $\phi_c = 90^\circ$ ,  $\theta = 90^\circ$

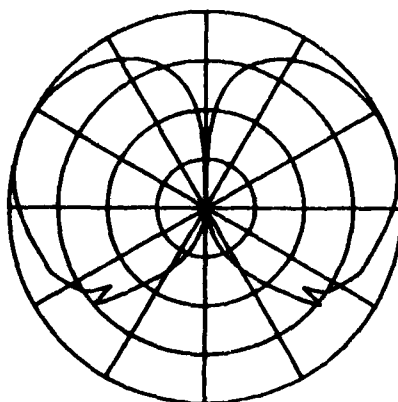


(b)  $\theta_c = 30^\circ$ ,  $\phi_c = 90^\circ$ ,  $\theta = 90^\circ$

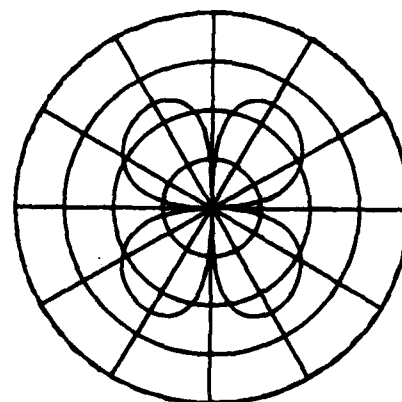


(c)  $\theta_c = 60^\circ$ ,  $\phi_c = 90^\circ$ ,  $\theta = 90^\circ$

—  $E_\phi$   
- - -  $E_\theta$

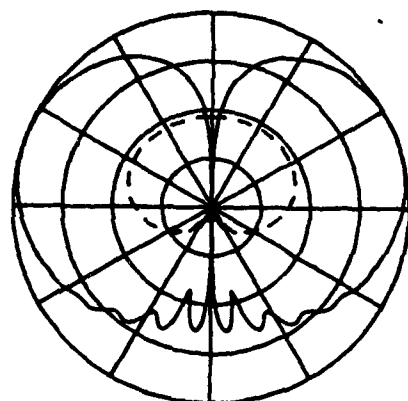


(d)  $\theta_c = 90^\circ$ ,  $\phi_c = 90^\circ$ ,  $\theta = 90^\circ$

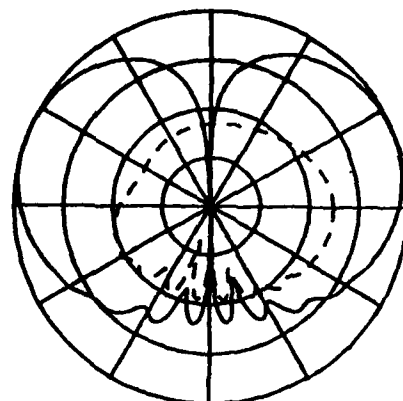


(e)  $\theta_c = 90^\circ$ ,  $\phi_c = 0^\circ$ ,  $\theta = 90^\circ$

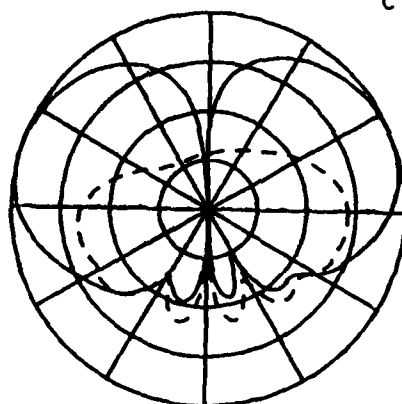
Figure 29. Radiation patterns for a short monopole mounted at  $\theta_s = 90^\circ$  on a  $2\lambda \times 4\lambda$  spheroid.



(a)  $\theta_c = 0^\circ$ ,  $\phi_c = 90^\circ$ ,  $\theta = 90^\circ$

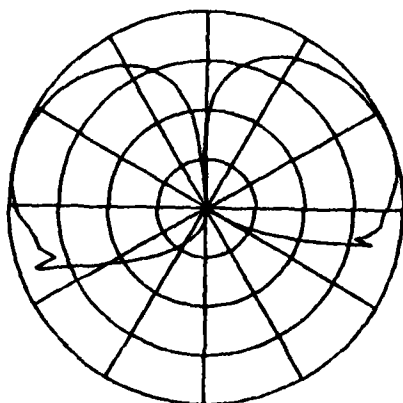


(b)  $\theta_c = 30^\circ$ ,  $\phi_c = 90^\circ$ ,  $\theta = 90^\circ$

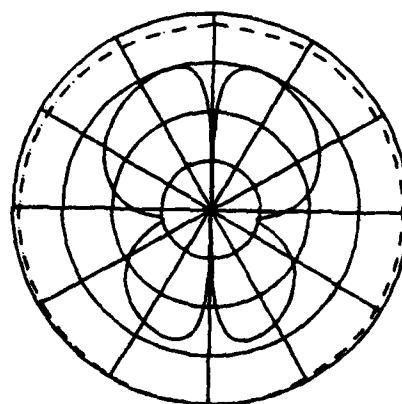


(c)  $\theta_c = 60^\circ$ ,  $\phi_c = 90^\circ$ ,  $\theta = 90^\circ$

—  $E_\phi$   
- - -  $E_\theta$

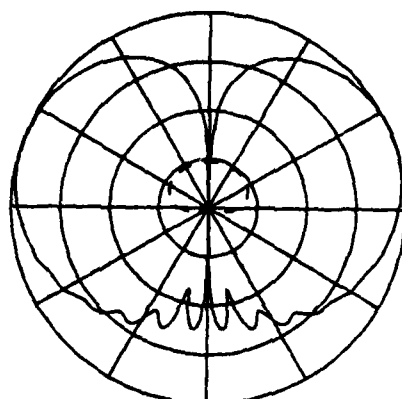


(d)  $\theta_c = 90^\circ$ ,  $\phi_c = 90^\circ$ ,  $\theta = 90^\circ$

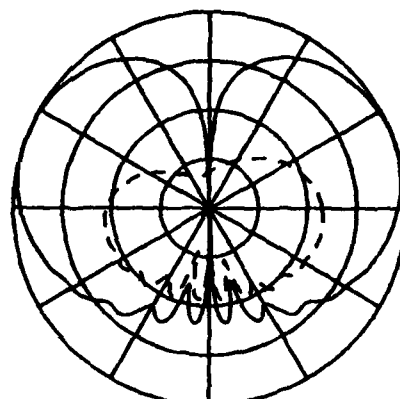


(e)  $\theta_c = 90^\circ$ ,  $\phi_c = 0^\circ$ ,  $\theta = 90^\circ$

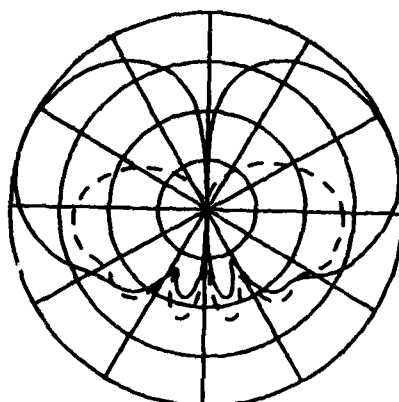
Figure 30. Radiation patterns for a short monopole mounted at  $\theta_s = 30^\circ$  on a  $2\lambda \times 10\lambda$  spheroid.



(a)  $\theta_c = 0^\circ$ ,  $\phi_c = 90^\circ$ ,  $\theta = 90^\circ$

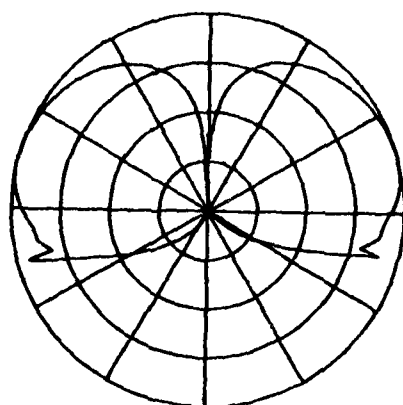


(b)  $\theta_c = 30^\circ$ ,  $\phi_c = 90^\circ$ ,  $\theta = 90^\circ$

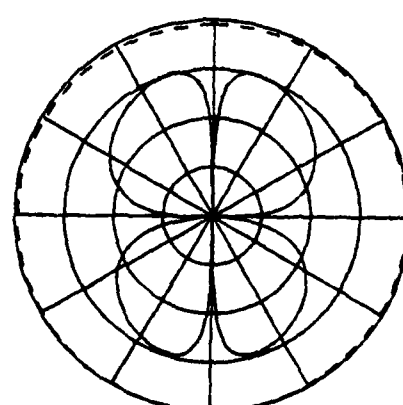


(c)  $\theta_c = 60^\circ$ ,  $\phi_c = 90^\circ$ ,  $\theta = 90^\circ$

—  $E_\phi$   
- - -  $E_\theta$

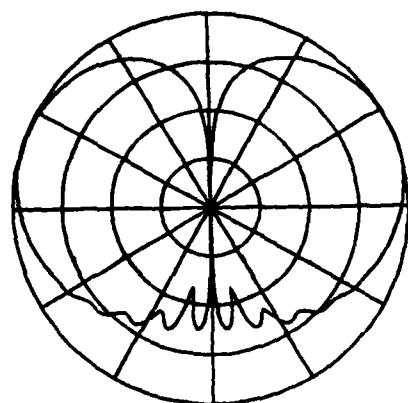


(d)  $\theta_c = 90^\circ$ ,  $\phi_c = 90^\circ$ ,  $\theta = 90^\circ$

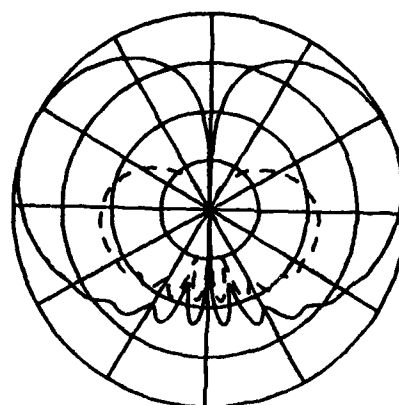


(e)  $\theta_c = 90^\circ$ ,  $\phi_c = 0^\circ$ ,  $\theta = 90^\circ$

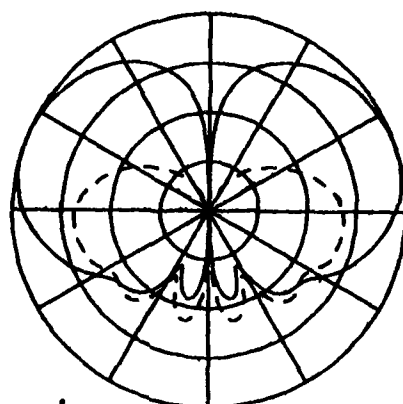
Figure 31. Radiation patterns for a short monopole mounted at  $\theta_s = 60^\circ$  on a  $2\lambda \times 10\lambda$  spheroid.



(a)  $\theta_c = 0^\circ$ ,  $\phi_c = 90^\circ$ ,  $\theta = 90^\circ$

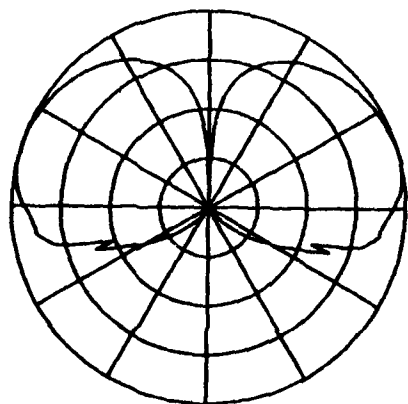


(b)  $\theta_c = 30^\circ$ ,  $\phi_c = 90^\circ$ ,  $\theta = 90^\circ$

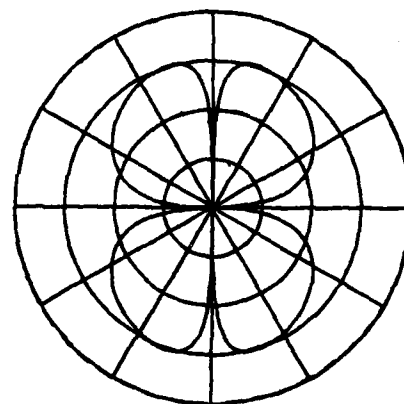


(c)  $\theta_c = 60^\circ$ ,  $\phi_c = 90^\circ$ ,  $\theta = 90^\circ$

—  $E_\phi$   
- - -  $E_\theta$



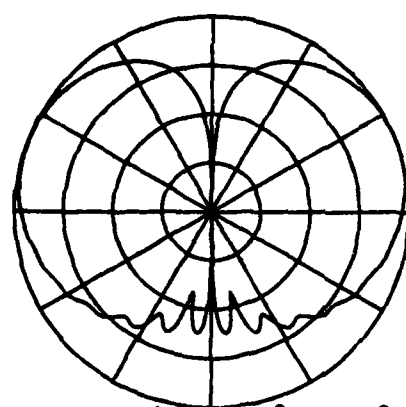
(d)  $\theta_c = 90^\circ$ ,  $\phi_c = 90^\circ$ ,  $\theta = 90^\circ$



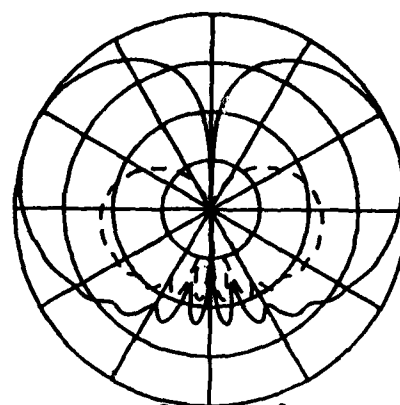
(e)  $\theta_c = 90^\circ$ ,  $\phi_c = 0^\circ$ ,  $\theta = 90^\circ$

Figure 32. Radiation patterns for a short monopole mounted at  $\theta_s = 90^\circ$  on a  $2\lambda \times 10\lambda$  spheroid.

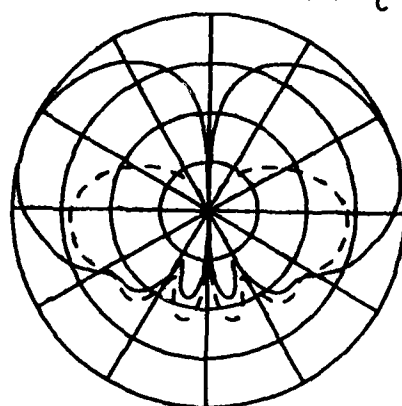




(a)  $\theta_c = 0^\circ$ ,  $\phi_c = 90^\circ$ ,  $\theta = 90^\circ$

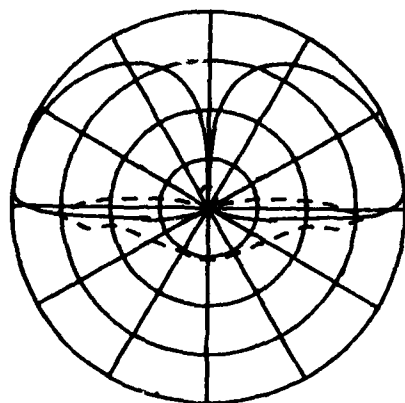


(b)  $\theta_c = 30^\circ$ ,  $\phi_c = 90^\circ$ ,  $\theta = 90^\circ$

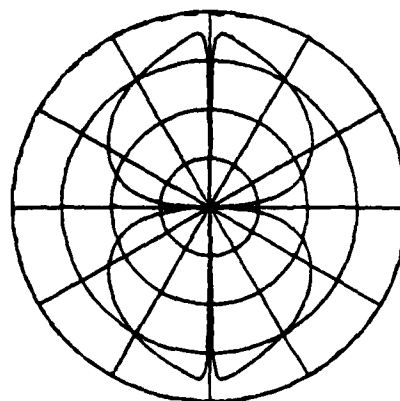


(c)  $\theta_c = 60^\circ$ ,  $\phi_c = 90^\circ$ ,  $\theta = 90^\circ$

—  $E_\phi$   
- - -  $E_\theta$

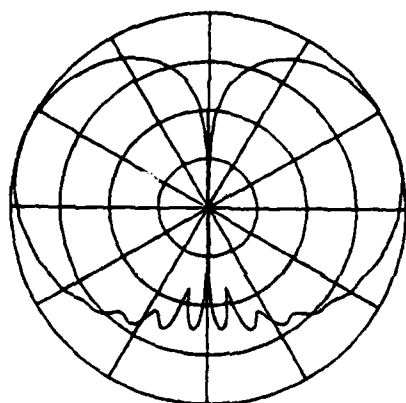


(d)  $\theta_c = 90^\circ$ ,  $\phi_c = 90^\circ$ ,  $\theta = 90^\circ$

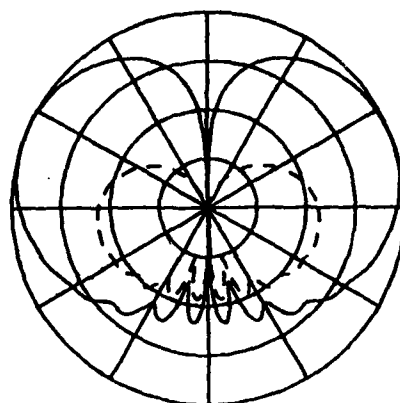


(e)  $\theta_c = 90^\circ$ ,  $\phi_c = 0^\circ$ ,  $\theta = 90^\circ$

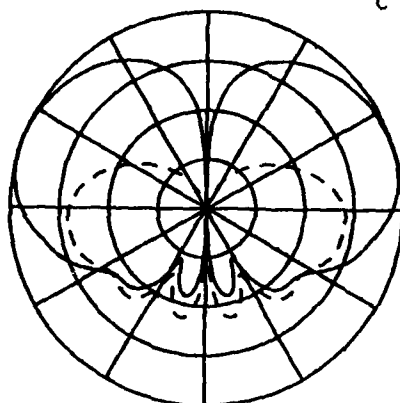
Figure 33. Radiation patterns for a short monopole mounted at  $\theta_s = 30^\circ$  on a  $2\lambda \times 50\lambda$  spheroid.



(a)  $\theta_c = 0^\circ$ ,  $\phi_c = 90^\circ$ ,  $\theta = 90^\circ$

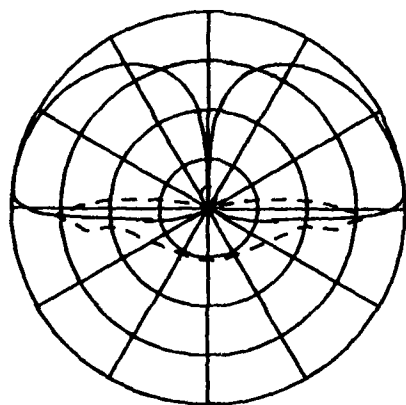


(b)  $\theta_c = 30^\circ$ ,  $\phi_c = 90^\circ$ ,  $\theta = 90^\circ$

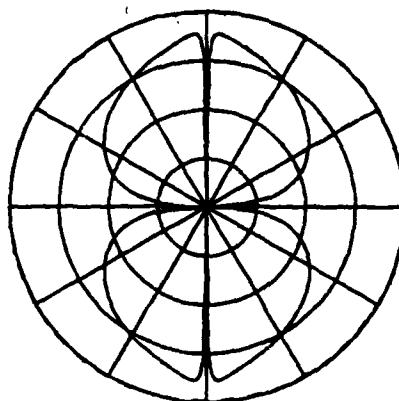


(c)  $\theta_c = 60^\circ$ ,  $\phi_c = 90^\circ$ ,  $\theta = 90^\circ$

—  $E_\phi$   
- - -  $E_\theta$

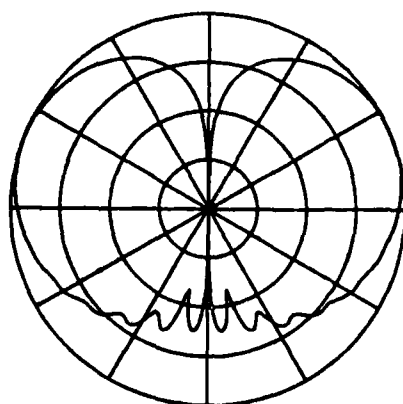


(d)  $\theta_c = 90^\circ$ ,  $\phi_c = 90^\circ$ ,  $\theta = 90^\circ$

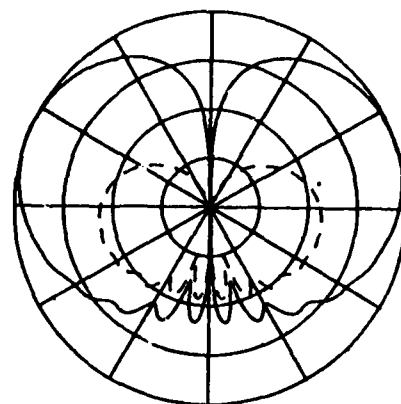


(e)  $\theta_c = 90^\circ$ ,  $\phi_c = 0^\circ$ ,  $\theta = 90^\circ$

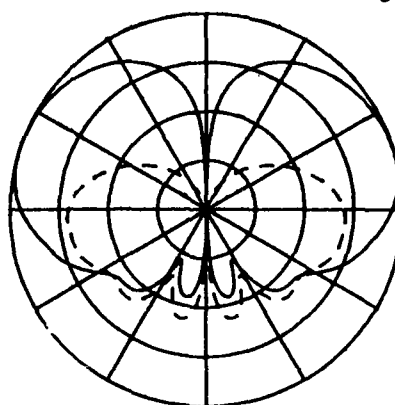
Figure 34. Radiation patterns for a short monopole mounted at  $\theta_s = 60^\circ$  on a  $2\lambda \times 50\lambda$  spheroid.



(a)  $\theta_c = 0^\circ$ ,  $\phi_c = 90^\circ$ ,  $\theta = 90^\circ$

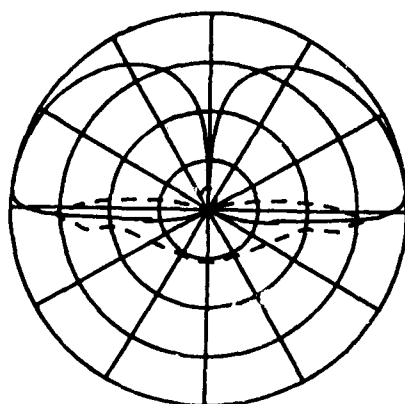


(b)  $\theta_c = 30^\circ$ ,  $\phi_c = 90^\circ$ ,  $\theta = 90^\circ$

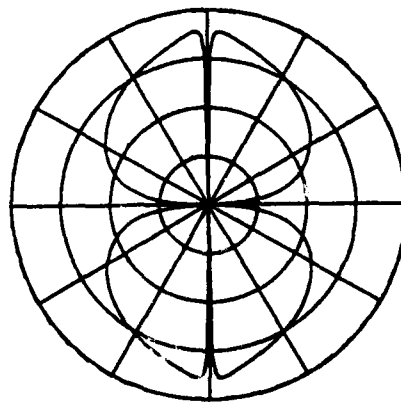


(c)  $\theta_c = 60^\circ$ ,  $\phi_c = 90^\circ$ ,  $\theta = 90^\circ$

—  $E_\phi$   
- - -  $E_\theta$



(d)  $\theta_c = 90^\circ$ ,  $\phi_c = 90^\circ$ ,  $\theta = 90^\circ$



(e)  $\theta_c = 90^\circ$ ,  $\phi_c = 0^\circ$ ,  $\theta = 90^\circ$

Figure 35. Radiation patterns for a short monopole mounted at  $\theta_s = 90^\circ$  on a  $2\lambda \times 50\lambda$  spheroid.

## CHAPTER V

### SUMMARY AND CONCLUSIONS

The object of this study has been to develop an efficient numerical solution for the high frequency radiation patterns of a spheroid-mounted antenna. The Geometrical Theory of Diffraction is used in this study to calculate the radiation patterns. The curved surface diffraction solutions are discussed in Chapter II, where the creeping wave solutions in the shadow region are of particular interest.

Cylinder and cone perturbation methods are presented in Chapter III to simulate the geodesic paths on a spheroid, which in turn can be used to model an aircraft or missile fuselage. Because the cylinder and cone are developed surfaces, the geodesic paths can be found on the unfolded planar surface. For a given radiation direction in the shadow region, the geodesic path and final diffraction point on the spheroid can, then, be found via an efficient numerical approach.

The Geometrical Theory of Diffraction is combined with the perturbation methods in Chapter IV to obtain various radiation patterns. The measured and calculated results are seen to agree very well except when a caustic comes into play. However, this type of caustic effect is still an unsolved problem and is beyond the scope of the present study.

These solutions are very useful in predicting the high frequency radiation patterns for antennas mounted on a spheroid. The cylinder and cone perturbation techniques are highly efficient in approximating the geodesic paths on the spheroid for this problem. Further, this perturbation method can be extended to more general convex surfaces such as ellipsoids.

## REFERENCES

1. Kouyoumjian, R.G., "Asymptotic High-Frequency Methods," Proc. of the IEEE, Vol. 53, No. 8, August 1965, pp.864-876.
2. Burnside, W.D., "Analysis of On-Aircraft Antenna Patterns," August 1972, Report No. 3390-1, The Ohio State University ElectroScience Laboratory, Department of Electrical Engineering, prepared under Contract No. 62269-72-C-0354 for Naval Air Development Center. Also a Dissertation to The Ohio State University, August 1972.
3. Pathak, P.H., Wang, N., Burnside, W.D., and Kouyoumjian, R.G., "A Uniform GTD Solution for the Radiation from Sources on a Convex Surface," February 1980, Report 711305, The Ohio State University ElectroScience Laboratory, Department of Electrical Engineering, prepared under Contract N00019-78-C-0524 for Department of Navy, Naval Air Systems Command.
4. Lipschutz, M.M., Differential Geometry, Schaum's Outline Series, McGraw-Hill Book Co., New York, N.Y., (1969).
5. Burnside, W.D., Wang, N., and Pelton, E.L., "Near Field Pattern Computations for Airborne Antenna," June 1978, Report 784685-4, prepared under Contract N00019-77-C-0299, Department of the Navy, Naval Air Systems Command.
6. Wang, N., "Near Field Solutions for Antennas on Elliptic Cylinder," July 1977, Report 784685-1, The Ohio State University Electro-Science Laboratory, Department of Electrical Engineering, prepared under Contract N00019-77-C-0299, Department of the Navy, Naval Air Systems Command.

